



New insights into the climatic signal from firn cores at the northern Antarctic Peninsula

Francisco Fernandoy¹, Dieter Tetzner², Hanno Meyer³, Guisella Gacitúa⁴, Kirstin Hoffmann³, Ulrike Falk⁵

5 ¹Facultad de Ingenieria, Universidad Andres Bello, Viña del Mar, 2531015, Chile

²Center for Climate and Resilience Research, University of Chile, Santiago, 8370361, Chile

³Alfred Wegener Institute Helmholtz Centre for Polar and Marine Research, Research Unit Potsdam, Telegrafenberg A43, 14473 Potsdam, Germany.

⁴Programa GAIA-Antártica, Universidad de Magallanes, Punta Arenas, 6210427, Chile

10 ⁵Climate Lab, Geography Depart., University Bremen, 28334 Bremen, Germany

Correspondence to: Francisco Fernandoy (francisco.fernandoy@unab.cl)

Abstract. The Antarctic Peninsula is one of the most challenging regions of Antarctica from a climatological perspective, owing to the recent atmospheric and oceanic warming. The steep topography and a lack of long-term and in situ meteorological observations complicate extrapolation of existing climate models to the sub-regional scale. Here, we present new evidence from the northern Antarctic Peninsula to demonstrate how stable water isotopes of firn cores and recent precipitation samples can reveal climatic processes related to nearby oceanic and atmospheric conditions. A noticeable effect of the sea ice cover on local temperatures and atmospheric modes, in particular the Southern Annular Mode (SAM), is demonstrated. In years with large sea ice extension in winter (negative SAM anomaly), an inversion layer in the lower troposphere develops at the coastal zone. Therefore, an isotope-temperature relationship valid for all seasons cannot be concluded. The δ -T. relationship rather depends on seasonal variability of oceanic conditions. Transitional seasons (autumn and spring) are both stable seasons with an isotope-temperature gradient of $+0.69\text{‰ }^{\circ}\text{C}^{-1}$. The firn stable isotope composition reveals that the near-surface temperature at the Antarctic Peninsula shows a decreasing trend ($-0.33^{\circ}\text{C y}^{-1}$) between 2008 and 2014. Moreover, the deuterium excess (d_{excess}) has been demonstrated to be a reliable indicator of seasonal oceanic conditions, and therefore suitable to improve a firn age model based on seasonal d_{excess} variability. The annual accumulation rate in this region is highly variable, ranging between $1060 \text{ kg m}^{-2} \text{ y}^{-1}$ and $2470 \text{ kg m}^{-2} \text{ y}^{-1}$ from 2008 to 2014. The combination of isotopic and meteorological data is key for reconstructing recent climatic conditions with a high temporal resolution in polar regions where no direct observation exists.



1 Introduction

West Antarctica and especially the Antarctic Peninsula (API) have been in the scope of the scientific community due to the notable effects of the present warming on the atmosphere, cryosphere, biosphere and ocean. The increase of air temperatures along the West Antarctic coast (Bromwich et al., 2013) displays signs of a shifting climate system since the early 20th century (Thomas et al., 2009). Recently, rapid warming of both atmosphere and ocean is causing instability of ice shelves on West Antarctica, especially in some regions of the API (Pritchard et al., 2012). The collapse of ice shelves triggers an accelerated ice–mass flow and discharge into the ocean, as the ice shelves’ buttressing function gets lost. Several grounded tributary glaciers on API and in West Antarctica recently loose mass to the oceans at accelerated rates due to this phenomenon (Pritchard and Vaughan, 2007; Rignot et al., 2005; Pritchard et al., 2012), which in combination with surface snow melt, has contributed to a negative surface mass balance of the region (Harig and Simons, 2015; Seehaus et al., 2015; Dutrieux et al., 2014; Shepherd et al., 2012).

The API is losing ice mass at rate of around 27 (± 2) Gt year⁻¹ between 2002 and 2014, which combined with the mass loss over West Antarctica ice sheet of 121(± 8) Gt year⁻¹, surpasses the positive mass balance observed in East Antarctica (Harig and Simons, 2015). This demonstrates how sensitive the coastal region of West Antarctica reacts on increased air and sea surface temperatures (Bromwich et al., 2013; Meredith and King, 2005).

Surface snow and ice melt has significantly increased on the API during the last decades, representing up to 20% of the total surface melt area (extent) and 66% of the melt volume of whole Antarctica (Abram et al., 2013; Trusel et al., 2012; Kuipers Munneke et al., 2012). Regional positive temperatures detected by remote sensing techniques and ice core data reveal that melt events have been temporally more wide–spread since the mid–20th century, with some severe melt events during the first decade of the 21st century (Trusel et al., 2012). Increased surface melt and glacier calving may have an impact on the fresh water budget of the upper ocean layers and therefore on the biological activity of the coastal zone (Meredith et al., 2016; Dierssen et al., 2002). The most significant warming trend detected at the coast of the API occurs during winter season, especially on the west side of the Peninsula, where a tendency $>0.5^{\circ}\text{C decade}^{-1}$ for the period 1960–2000 has been reported for several stations (Turner et al., 2005; Carrasco, 2013). Winter warming is especially evident on the daily minimum and monthly mean temperature increase, as described by Falk and Sala (2015) for the meteorological record of the Bellingshausen Station at King George Island (KGI) at the northern API during the last 40 years. In KGI the daily mean temperature during winter increased at about $0.4^{\circ}\text{C decade}^{-1}$, with highly marked warming during August at a rate of $+1.37(\pm 0.3)^{\circ}\text{C decade}^{-1}$. Therefore, positive temperatures even in winter are more commonly observed, leading to more frequent and extensive surface melting year–round especially for the northern API, which is dominated by maritime climate conditions (Falk and Sala, 2015). The mechanisms behind increasing atmosphere and ocean temperatures are still not completely understood but can be confidently linked to perturbations of typical atmospheric circulation patterns (Pritchard et al., 2012; Dutrieux et al., 2014). Most heat advection to the southern ocean and atmosphere has been related to the poleward movement of the southern oscillation or Southern Annular Mode (SAM) and to some extent to the El Niño Southern Oscillation (ENSO) (Gille, 2008;



5 Dutrieux et al., 2014; Fyfe et al., 2007). During the last decades, SAM has been shifting into a positive phase, implying lower than normal (atmospheric) pressures at coastal Antarctic regions (latitude 65°S) and higher (atmospheric) pressures over mid-latitudes (latitude 40°S) (Marshall, 2003). With lower pressures around Antarctica, the circumpolar westerly winds increase in intensity (Marshall et al., 2006). Air masses transported by intensified westerlies overcome the topography of the API more frequently, especially in summer, bringing warmer air to the east side of the API. The relationship between the shift of the SAM and the surface air temperature trend is generally positive for the API, explaining a large part (~50%) of near-surface temperature increase for the last half century (Marshall et al., 2006; Marshall, 2007; Carrasco, 2013; Thompson and Solomon, 2002). An enhanced circulation allows more humidity to be transported to and trapped at the west coast of the API due to the orographic barrier of the central mountain chain. Therefore, the accumulation has consistently increased across the entire Peninsula during the whole 20th century, doubling the accumulation rate from the 19th century in the southern API region (Thomas et al., 2008; Goodwin et al., 2015; Dalla Rosa, 2013).

The increase of greenhouse gas concentrations and the stratospheric depletion of the ozone layer, both linked to anthropogenic activity, are suggested to be the main forcing factors of the climate shift that affects the ocean-atmosphere-cryosphere system for at least the last half century (Fyfe and Saenko, 2005; Sigmond et al., 2011; Fyfe et al., 2007).

15 The lack of long-term meteorological records hampers to accurately determine the onset and regional extent of this climate shift. Therefore, climate models were improved and used to extend the scarce climate data both spatially and temporally. One major challenge is to correctly integrate the steep and rough topography of the API into climate models. To realize this goal, direct information on surface temperature, melting events, accumulation rates, humidity sources and transport paths are urgently needed. As direct measurements of these parameters are not available, researchers must rely on the reconstruction of the environmental variability, mainly based on proxy data such as the stable water isotope composition of precipitation, firn and ice (e.g.: Thomas and Bracegirdle, 2009; Thomas et al., 2009; Abram et al., 2013).

In this investigation, we focus on a stable water isotope-based, high temporal resolution reconstruction of variables including accumulation rates, temperatures and melt events on the API and their relationship to atmospheric modes and moisture-source conditions i.e. sea surface temperature, humidity and sea ice extent.

25 Since 2008, we have undertaken several field campaigns to the northernmost region of the API, where we have retrieved a number of firn cores of up to 20 m depth. By using the stable water isotope composition of these cores as a proxy for the recent climate variability, we aim to fill the gap of lacking meteorological (in situ) observations. We have determined the effects of the orographic barrier of the API on the air mass and moisture transport, with increasing precipitation rates from the coast to the mountain range on the Peninsula divide at ca. 1100 m a.s.l. (Fernandoy et al., 2012), where the ice thickness reaches ca. 30 350 m at its highest surface point (Cárdenas et al., 2014) .



2 Methodology

2.1 Field work and sample processing

During five summer campaigns (2008–2010, 2014, 2015) several shallow–depth firn cores (totaling more than 60 m) were retrieved from the northern part of the API. An altitudinal profile was completed from sea level near O'Higgins Station (OH) to 1130 m a.s.l at the Laclavere Plateau (LCL). In total, five firn cores were included in this paper: OH-4, OH-5, OH-6, OH-9, OH-10 (Fig. 1); coordinates and further details of the firn cores are given in Table 1. More than 200 daily precipitation samples were gathered from O'Higgins Station (57.90°W, 63.32°S, 13 m a.s.l.) during 2008–2009 (Fernandoy et al., 2012) and 2014 (Table 2). Some of these samples were discarded from the analysis due to improper storing. Cores OH-4, OH-5, OH-6 and OH-9 were retrieved between 2008 and 2010 and analyzed for their stable water isotope composition and physical properties as described in Fernandoy et al. (2012) and Meyer et al. (2000). Additionally, a density profile of OH-9 was obtained by using an X-ray microfocus computer tomograph at the ice core processing facilities of the Alfred Wegener Institute, Helmholtz Centre for Polar and Marine Research in Bremerhaven, Germany (Linow et al., 2012). The X-ray tomography provides a very high–resolution (1mm) density profile of the physical properties of the ice. The core OH-10 was retrieved in 2015 using an electric drilling device with 5.7 cm inner diameter (Icedrill.ch AG). The retrieved core was first stored under controlled temperature conditions (-20°C) at the Chilean scientific station Prof. Julio Escudero (King George Island) and later transported to a cold storage in Viña del Mar, Chile. The core sections were measured and weighted for density–profile construction and then sub–sampled with a 5 cm resolution for stable water isotope analysis. A visual logging and description of the cores were carried out to identify possible melt layers and their thicknesses. Thereafter, firn and recent precipitation samples collected from OH in 2014 were analyzed by a liquid water stable isotope analyzer from Los Gatos Research (TLWIA 45EP), located at the Stable Isotope Laboratory of the Universidad Nacional Andrés Bello, Viña del Mar, Chile. Accuracy of the measurements is better than 0.1 ‰ for oxygen and 0.8 ‰ for hydrogen isotopes.

2.2 Database and time series analysis

Stable water isotope data were compared to major meteorological parameters from the region (Fig. 2). For this purpose, the following data sets were incorporated into our analysis: Near–surface air temperature (T_{air}), precipitation amount (Pp) and sea–level pressure (SLP), recorded at the Russian Station Bellingshausen (BE) (58.96°W, 62.19°S, 15.8 m a.s.l.), available in daily and monthly resolution from the Global Summary of the Day (GSOD) data sets of the National Climatic Data Center (NCDC, available at: www.ncdc.noaa.gov) and the SCAR Reference Antarctic Data for Environmental Research (READER, available at: www.antarctica.ac.uk/met/READER/) (Turner et al., 2004). Sea surface temperature (SST) time series were extracted from the Hadley Centre Sea Ice and Sea Surface Temperature data set (HadISST, available at: <http://hadobs.metoffice.com/hadisst/>). The HadISST provides SST monthly means on a global 5° to 5° grid from 1973 to present (Rayner et al., 2003). Mean monthly SSTs were extracted from a quadrant limited by 60–65°S and 65–55°W. Missing data or outliers were interpolated from measurements taken in the neighbor quadrants. Relative humidity (rh) time series were extracted from data obtained by the



calculation of 3 day air parcel backward trajectories under isobaric conditions using the freely-accessible Hybrid single-particle Lagrangian integrated trajectory (HYSPLIT) model (Draxler and Hess, 1998, available at: <http://ready.arl.noaa.gov/HYSPLIT.php>). This three-dimensional model was fed with the global data assimilation system (GDAS) archives from NOAA/NCEP (Kanamitsu, 1989). GDAS offers a global 1° to 1° latitude-longitude spatial coverage with a 1 hour temporal resolution and is available from 2006 to present (for more details visit: <http://ready.arl.noaa.gov/gdas1.php>). For studying the characteristics of air parcels approaching API, *rh* time series were obtained considering data from 1 day backward trajectories. SST and *rh* datasets were resampled to a regional scale defined by high-density trajectory paths (Bellingshausen and Weddell Seas). The resampled fields were defined by the spatial coverage of 1 day backward trajectories. The limits of the resulting quadrant extends from 98° W to 34° W longitude and from 47° S to 76° S latitude. A field horizontal mean of resampled *rh* values between sea level and 150 m a.s.l. was computed to construct *rh* time series utilized throughout this work. Altitudinal temperature profiles were obtained from radiosonde measurements carried out at BE between 1979 and 1996 (SCAR Reference Antarctic Data for Environmental Research). Lapse rates were calculated from the temperature difference between sea level and the 850 hPa level. SAM index time series were obtained from the British Antarctic Survey (BAS, available at: <http://legacy.bas.ac.uk/met/gjma/sam.html>) (Marshall, 2003). Mean monthly sea ice extent around the API (between 1979 and 2014) was obtained from the Sea Ice Index from the National Sea & Ice Data Center (NSIDC, available at <http://nsidc.org>).

2.3 Stable Isotope time series analysis

For each precipitation event registered at OH, a 3 day air parcel backward trajectory was calculated to identify *rh* conditions above sea level in the ocean near the API. For this purpose we used the HYSPLIT model (Draxler and Hess, 1998) with hourly temporal resolution. Frequent air parcel paths were studied and monthly mean values of *rh* and SST were calculated. Using the relationship between *rh* and SST calculated by Uemura et al. (2008), a theoretical value of deuterium excess ($d_{excess\ meteo}$) was calculated for the whole region ($d_{excess\ meteo} = -0.42 * rh + 0.45 * SST + 37.9$). Comparisons were made between time series of deuterium excess ($d_{excess} = \delta D - 8 * \delta^{18}O$), obtained from monthly mean values of the precipitation isotopic signal, and $d_{excess\ meteo}$, obtained from monthly mean values of *rh* and SST from the southern oceans.

Simultaneously, the d_{excess} signal obtained from stable isotope analysis of firn cores was transformed into a signal depicted with depth. Then it was filtered using the Inverse Fast Fourier Transform (IFFT), which was fed with the frequency of the second of the principal modes of oscillation obtained from the Fast Fourier Transform (FFT). Thus, the final signal is only defined by the low frequencies. The same procedure was applied to the time series constructed with monthly means of $d_{excess\ meteo}$. The strong similarities between both signals, due to their dependency on the same variables, enables the transformation from the depth domain of the d_{excess} stable isotope signal to the time domain by using the common principal oscillation patterns as time markers. As d_{excess} is now represented in the time domain (Fig. 3), monthly means were calculated to generate time series for further analysis. Once the d_{excess} signals from firn cores were represented as time series, the same procedure was



followed to generate $\delta^{18}\text{O}$ time series (Fig. 3). The $\delta^{18}\text{O}$ – Temperature relationship was obtained from precipitation samples and daily mean temperatures at OH.

2.4 Complementing geophysical data

Ground-penetrating radar (GPR) is a geophysical method based on the propagation and reflection of electromagnetic waves (Annan and Davis, 1976). Reflections are produced when dielectric discontinuities are reached in the propagation media. GPR has been proved to be effective in dry snow layer interpretation where reflections are most commonly produced from internal density differences (Spikes et al., 2004). Therefore, GPR data complement ice-core interpretations, allowing the spatial extrapolation of ice-core layer detection and evaluation of layer continuity.

GPR measurements were performed during the OH-10 firn core drilling campaign in January 2015. We used a SIR3000 unit equipped with a 400 MHz central frequency antenna (GSSI Inc.), that was dragged in a sledge along the proposed measurement lines (Fig. 4). The penetration depth of the electromagnetic waves is strongly controlled by the electrical conductivity of the propagation medium (i.e. snow) as well as by the central frequency of the system (Daniels, 2007), which decreases as frequency increases. The used system provides a good compensation between these parameters, where the vertical resolution in dry polar snow is approximately 0.35 m reaching up to 100 m in depth (Spikes et al., 2004). However, these values are variable for snow/firn in low polar latitudes (e.g. Antarctic Peninsula), where the range for layer detection increases and the maximum depth decreases.

Raw radar data were processed and interpreted using the software Reflexw (<http://www.sandmeier-geo.de>). Each radar profile was manually georeferenced using differential global positioning system (DGPS) data collected during the GPR measurements. Prior to the snow/firn stratigraphy interpretation from radar imaging, processes and corrections included removal of repetitive traces and application of filters to diminish signal noise (e.g. frequency filter, deconvolution and stacking). Each collected file was analyzed independently and layers were distinguished and chosen manually. Thus, if layers were not sufficiently clear and continuous, the files were not picked (Fig. 5). Data was further analyzed in the ASCII format (i.e. *easting, nothing, elevation, depth*).

3. Results

Oxygen and hydrogen stable water isotope data of precipitation and firn core samples are presented in relation to the Vienna Standard Mean Ocean Water Standard (VSMOW) in ‰, as $\delta^{18}\text{O}$ and δD for oxygen and hydrogen isotopes, respectively.

3.1 Precipitation samples OH

Table 2 shows the stable isotope results and basic statistics for the precipitation samples collected at OH station. The comparison between δD and $\delta^{18}\text{O}$ from precipitation samples allows the definition of a Local Mean Water Line (LMWL) given



by the expression $\delta D = 7.83 * \delta^{18}O - 0.12$. Backward trajectory analysis for precipitation events reveals a high-frequency transport across the Bellingshausen Sea within the last 24 hours before the air parcels reach the API (Fig. 6).

3.1.1 Isotope – Temperature relationship

Using the stable water isotope composition of single precipitation events and daily near-surface temperature (T_{daily}), an isotope-temperature relationship was constructed for OH station using a linear regression analysis. For this purpose, each seasons' sample set was selected from the months with the largest number of samples (i.e. December 2008, March 2008–2009, June 2008 and October 2014). All comparisons between $\delta^{18}O$ and T_{daily} revealed correlation coefficients (R) higher than 0.6 and a statistical significance (p) lower than 0.03 for a total of 208 precipitation events analyzed. Outliers were discarded as explained in section 3.1.2. Furthermore, the same analysis was carried out using monthly averages calculated from daily events (T_{monthly}) from the whole precipitation dataset ($R= 0.5$, $p= 0.01$), considering a total of 24 months. Considerable differences were identified between the daily and monthly $\delta^{18}O$ - T relationships (Fig. 7a). The linear regression slope (s) of MAM (March-April-May), considering the March 2008–2009 dataset to be representative of the MAM behavior, has shown to be quite near to s of SON (September-October-November), considering the October 2014 dataset to be representative of the SON behavior: $s= 0.77$ and $s= 0.61$, respectively. If only the two datasets (MAM and SON) are taken into account, a new linear regression can be obtained as: $\delta^{18}O= 0.69* T_{\text{daily}}+4.43$ ($R= 0.74$, $p<0.01$). Thus, the time series of monthly averages shows a direct relation between both parameters. An inverse behavior of s was identified during July 2008 and June 2014.

3.1.2 Deuterium excess – Temperature relationship

From stable water isotope results obtained from precipitation samples, d_{excess} values were calculated for each sample. Table 2 shows d_{excess} basic statistics for the dataset. The d_{excess} values lower than -2.0 ‰ were filtered in order to avoid disturbances, as these samples might have been influenced by secondary processes during storage and transport. Daily d_{excess} values for the same months as specified in section 3.1.1 were compared with daily mean temperatures. Correlation coefficients for these comparisons are weak ($R<-0.42$, $p>0.1$) and broadly scattered. The comparison considering monthly averages calculated from daily events from the whole dataset improved the $d_{\text{excess}} - T$ correlation coefficient ($R= -0.71$, $p<0.01$; $T= -0.98 * d_{\text{excess}} - 0.33$) (Fig. 7b). Time series of monthly averages show a clear inverse relationship between both parameters for the whole dataset.

3.1.3 Moisture source of precipitation

Air backward trajectories from precipitation events exhibit a wide spatial distribution, including the South Pacific Ocean and the Amundsen–Bellingshausen Seas. The trajectories are mainly distributed in the Bellingshausen Sea, the Bransfield Strait and the Drake Passage, partially including Tierra del Fuego and South America's southern tip, although some trajectories ($<15\%$) originate from API's eastern side. Precipitation trajectories show an almost $N40^\circ W$ elliptically distributed pattern where most of them follow pathways restricted between latitudes $60^\circ S$ and $67^\circ S$. From the relationship between monthly mean



values of d_{excess} from precipitation samples and $d_{excess\ meteo}$ constructed from meteorological parameters (rh and SST) of the high density precipitation pathways, a correlation coefficient of $R= 0.86$ ($p<0.01$) was obtained (Fig. 8).

3.2 Firn core samples from API

Table 1 shows the stable isotope results and basic statistics for firn cores retrieved at the northern API. The co-isotopic relationship $\delta D - \delta^{18}O$ of each single firn cores retrieved from LCL is close to the GMWL and LMWL, with a mean slope of $m= 7.91$ and an intercept of 3.64 (Fig. 9). These values are very close to those of the LMWL, although with a slightly higher intercept.

3.2.1 Age model based on stable water isotope and geophysical data

Stable water isotope results from firn cores allowed to derive depth profiles of δD , $\delta^{18}O$ and d_{excess} for each firn core. Lower noise and the clearest seasonal pattern was found in d_{excess} profiles ($d_{excess\ core}$) (Fig. 3), similar to findings published by Fernandoy et al. (2012). The $d_{excess\ core}$ signals were analyzed by filtering their high frequency oscillation patterns and comparing the remnant signals with $d_{excess\ meteo}$ monthly means, which prevail on the high density pathways, covered by air parcels that reach LCL surroundings within 2 days. Main peak-valley fitting between both signals led to a monthly mean $d_{excess\ core}$ signal represented on a time scale. The comparison between time series of monthly mean $d_{excess\ core}$ and $d_{excess\ meteo}$ data reveals correlation coefficients of $R\geq 0.67$ ($p<0.01$) for all firn cores analyzed and obtained from 2006 to 2015. Table 3 summarizes correlation coefficients, statistical significances and time intervals covered by each firn core. From the firn cores retrieved from LCL, a single time series was constructed and then compared to the $d_{excess\ meteo}$ time series in order to analyze the isotopic signal along the whole time interval. A correlation coefficient of $R= 0.75$ ($p<0.01$) was obtained between the two signals ($d_{excess\ meteo}$ and $d_{excess\ core}$). To construct one single time series from the firn cores, on the overlapping time interval between OH-9 and OH-10 (February 2012 to January 2014), we only considered data from OH-9, because the samples from OH-9 consists of more fresh and less compacted firn than the respective interval in OH-10. This in turn helps to avoid attenuation of the isotopic signal. Although we only considered OH-9 data for the overlapping time interval, we studied the changes in the standard deviation of the isotopic signal in both firn cores in the common time span. The standard deviation shows a decrease of 16% after one year of deposition in core OH-10 with respect to the same time interval in OH-9; and 2 to 3 years after the deposition the smoothing of the signal increased up to 18%.

During firn core visual logging, thin and scarce melt layers were identified (mean width of ~ 1 cm). The melt layers do not show evidence of infiltration nor have a clear pattern of distribution with depth (i.e. association with summer layers). While analyzing them in relation to their time equivalent with depth, no clear pattern associated with a season was noted.

3.2.2 Seasonal temperature reconstruction from stable water isotope ratios

The age model developed using the $d_{excess\ core}$ oscillation was later applied to construct a $\delta^{18}O$ time series (Fig. 3). From this time series a periodical 2 year pattern was identified. This pattern is characterized by elevated values, higher than the $\delta^{18}O$



mean, between May and November in the years 2008, 2010, 2012 and 2014, which exhibit an inverse relationship to temperature at BE. Between June and July in the following years 2009, 2011 and 2013, $\delta^{18}\text{O}$ values are lower than the mean and exhibit a direct relationship to temperature at BE (Fig. 10). Monthly mean $\delta^{18}\text{O}$ values were transformed to their temperature equivalent using the $\delta^{18}\text{O} - T$ relationship obtained in section 3.1.1 from precipitation samples (Fig. 11). Monthly $\delta^{18}\text{O} - T$ relationship was considered to reflect seasonal behavior. As seasonal behavior differences were found to be more pronounced during different years, for those cases the use of certain $\delta^{18}\text{O} - T$ relationship were extended or contracted considering MAM-ON (March 2008–2009, October 2014), JJAS (June 2008) and DJF (December 2008). Despite this main seasonal classification for the use of $\delta^{18}\text{O} - T$ relationship, some particular seasons showed variable behavior with respect to the general trend during specific years. In those cases, the seasonal behavior was extended or contracted beyond the boundaries of the main season classification depending on sea ice extent. Large sea ice extent during winter, will lead to a delayed on-set of spring conditions. In this case winter-like conditions will be extended beyond August. Restricted sea ice extent on the contrary will lead to earlier spring-like conditions (before August).

Additionally, the relationship between monthly lapse rates in BE, winter SAM index and sea ice extent (SIE) from OH is represented in Fig. 12a. As temperature data from OH show several large record gaps, for the estimation of air temperature on LCL, we considered the BE temperature corrected by a latitude factor (-1.4°C). Considering latitude-corrected air temperatures from BE, lapse rates from BE and SIE from OH (SIE_{OH}), a mean annual air temperature of -7.5°C with a trend of $-0.18^\circ\text{C year}^{-1}$ was estimated on LCL for the time period 2009-2014 (Fig. 12b). A monthly temperature mean estimate, derived from the linear correlation between meteorological data and the monthly $\delta^{18}\text{O} - T$ relationship, can be expressed by the equation $T_{\text{LCL}} = (T_{\text{BE}} - 1.4) + 1.13 (M_{\text{month}} * \text{SIE}_{\text{OH}} + N_{\text{month}})$, where M_{month} and N_{Month} represent the slope and intercept of the monthly $\delta^{18}\text{O} - T$ relationship, respectively. Additionally, considering the $\delta^{18}\text{O}$ time series data and the isotope - T relationship, a mean annual air temperature of -6.5°C with a trend of $-0.33^\circ\text{C year}^{-1}$ was estimated on LCL for the years 2009-2014. The comparison between monthly mean temperature on LCL, estimated using the $\delta^{18}\text{O}$ signal from firn cores and T_{LCL} estimated using the coupled effect of the latitude-corrected temperature record from BE, SIE_{OH} and lapse rates from BE, reveals a correlation coefficient of $R = 0.7$ ($p < 0.01$). Both signals show a synchronous behavior, also with respect to the air temperature record at OH station. No statistically significant direct correlation was observed between coastal station temperature records and the stable water isotope composition of firn cores.

Comparing the $\delta^{18}\text{O}$ signal from OH-6 with data from precipitation samples at OH and with two other cores from the western side of the API (OH-4 and OH-5) during a common period (March 2008 – August 2008), a $\delta^{18}\text{O}$ decrease of -0.08‰ km^{-1} was found with increasing distance from the coast (Figure 13a). The same data set was used to study the $\delta^{18}\text{O} - \text{altitude}$ relationship. The $\delta^{18}\text{O}$ seasonal means show altitude dependence through which seasonal $\delta^{18}\text{O} - \text{altitude}$ patterns could be distinguished. During MAM a clear decreasing rate of -2.4‰ km^{-1} from sea level up to LCL is found, whereas during JJA no clear decreasing $\delta^{18}\text{O}$ trend is obtained from sea level up to 1130 m a.s.l. (Figure 13b).



3.2.3 Accumulation rates

Density measurements from firn cores were used to construct density–depth profiles. Along those profiles a clear trend of increasing density with depth was obtained. Linear regressions across different sections represent a normal firn compaction process reaching the snow–firn–density boundary (550 g cm^{-3}) at 15.2 m depth. Using these linear regressions and considering the depth intervals delimited in section 3.2.1 as monthly values, we were able to estimate accumulation rates during different periods. By using this procedure, we have estimated accumulation rates at LCL between 2008 and 2015, with a mean accumulation of $1770 \text{ kg m}^{-2} \text{ y}^{-1}$. The highest value was found in 2008 ($>2470 \text{ kg m}^{-2}$), then the accumulation rate noticeably decreased until 2015 (1600 kg m^{-2}) reaching its lowest absolute value in 2010 (1060 kg m^{-2}) (Fig. 14a). A seasonal trend was observed, reflecting a decrease in the accumulation during JJA and SON between 2008 and 2015, which is responsible for the overall decreasing rates. On the other hand, the highest accumulation occurs during MAM and SON seasons (Table 4). Accumulation rate estimations derived from cores OH-9 and OH-10 for 2012 – 2013 (common period) differ only by about 3%. Other cores from the west flank of the Peninsula (OH-4, OH-5 and OH-6) show that the accumulation in 2008 (common period) depends on the altitude, with increasing values from the lower region to the highest point on LCL (Fig. 14b). The increase rate is about $1500 \text{ kg m}^{-2} \text{ km}^{-1} \text{ y}^{-1}$ from 350 m a.s.l. to 1130 m a.s.l.

3.2.4 GPR data interpretation around OH-10 site

GPR electromagnetic waves are reflected from the dielectric interfaces produced when seasonal snow is accumulated (Arcone, 2009). However, low compaction between recent years of accumulated snow at LCL prevented the detection of snow stratigraphy in depths less than ~ 7 m. The minimum depth of a continuous layer observed was 7.4 m and the deepest layer reached up to 41.8 m below the surface. Wind circulation from the northwest cause wind erosion and thus hamper layer detection. Therefore, layer density and continuity were less visible at the northwest side. The minimum number of detected layers by GPR section was 9, and the maximum was 16 (Figure 5). Referring to the isotope–based dating of the OH-10 core, the GPR signal indicates that at the OH-10 site, 7.4 m of accumulated snow corresponds to January 2013. Consequently, the deepest layer detected corresponds to the austral summer of 1998 (~ 41 m snow/firn accumulation in 16 years).

4 Discussion

4.1 Stable water isotope fractionation processes and the local temperature relationship

The stable water isotope composition of precipitation samples from the 2008 and 2014 datasets show a high similarity to each other, as well as to firn cores from the western flank and from LCL Plateau at API (OH-4 to OH-10), and to several meteorological and climatic parameters and reanalysis data. Backward trajectory analysis revealed that the most frequent pathways for air parcels that reach the northern part of API derive from the Bellingshausen Sea, between 55°S and 60°S (Fig.



6) throughout the year. In contrast, localities further south on the API and in West Antarctica, Ellsworth Land and coastal Ross Sea, respectively, exhibit a stronger continental influence on the precipitation source, depending on seasonal and synoptic scale conditions (Thomas and Bracegirdle, 2015; Sinclair et al., 2012). The LMWL obtained from precipitation samples at OH ($m=7.83$) is closely related to the Antarctic meteoric water line obtained by Masson-Delmotte et al. (2008) ($m=7.75$), and to the GMWL as presented by Rozanski et al. (1993) ($m=8.13$). The similarity between the slope of LMWL and GMWL indicates that the fractionation processes during condensation mostly take place under thermodynamic equilibrium (Moser and Stichler, 1980). These results are consistent with those obtained by other authors for King George Island (Simões et al., 2004; Jiahong et al., 1998). Moreover, by combining the stable water isotope signature of OH precipitation with time series of meteorological data representative for the conditions prevailing on the ocean near OH station, a strong relationship with rh and SST at the moisture source can be derived. This relationship has been well established, especially for the coastal Antarctic region where moisture transport from the source is generally short-ranging (Jouzel et al., 2013). The comparison between the d_{excess} of precipitation and the theoretical $d_{excess\ meteo}$ derived from time series of meteorological data from the surrounding region has shown that both datasets are highly correlated ($R=0.86$). Based on this evidence, we suggest that the Bellingshausen Sea constitutes the most important source of water vapor for precipitation at the API. Some precipitation events that exhibited a stable water isotope composition beyond the normal range for the region (e.g. 20 August 2009, $\delta^{18}O = -19.4\text{‰}$), were associated with uncommon sources of humidity as also recognized by the backward trajectory analysis.

The changing seasonal $\delta^{18}O - T$ relationship obtained from precipitation samples shows that the relationship between air temperature and condensation temperature varies throughout the year. The strong similarity in the $\delta^{18}O - T$ relationship during MAM and SON contrasts with the pronounced difference of this relationship between DJF and JJA. This highlights the variability of the $\delta^{18}O - T$ relationship along the whole year in this region. Nonetheless, the $\delta^{18}O - T$ relationships obtained for MAM and SON ($0.77\text{‰ }^{\circ}\text{C}^{-1}$ and $0.61\text{‰ }^{\circ}\text{C}^{-1}$, respectively) are similar to the values obtained by other authors for the API (Aristarain et al., 1986; Peel et al., 1988). Although the seasonal temperature difference is reduced in coastal sites, the difference in the seasonal $\delta^{18}O - T$ relationship suggests the existence of processes that disrupt the direct linkage between condensation temperature and surface air temperature. The inverse relationship between the $\delta^{18}O$ signal from LCL ice cores and BE (and OH) monthly mean temperatures (Fig. 11), which is noticeable in some years during JJA, contrasts with the commonly accepted seasonal behavior characterized by a direct relationship between $\delta^{18}O$ and surface air temperatures (Clark and Fritz, 1997). This particular behavior could be related to strong variations in meteorological conditions in the area between BE (OH) and LCL throughout the whole year. Therefore, air temperature on LCL was estimated by two independent methods: lapse rates (vertical temperature gradient) and $\delta^{18}O - T$ equivalents. The best correlation between both temperatures was obtained when an extended seasonal behavior was considered ($R=0.7$; $p<0.01$). This result is in agreement with the natural seasonal variability in high latitudes, where the effects of some seasons extend beyond the theoretical seasonal temporal limits, as previously explained. Failing to take this seasonal variability into account would lead to a misinterpretation of the air temperature reconstruction for LCL, since then the $\delta^{18}O - T$ correlation would be rather poor ($R=0.42$) and would not reflect the true seasonality in this region. The high similarity in $\delta^{18}O - T$ relationship during MAM and SON can be explained by the



seasonal transition between summer and winter, when oceans surrounding the northern API pass from ice-free to fully ice-covered conditions, respectively. Likely, ice-free ocean conditions are related to natural seasonal oscillations, which are highly dependent on atmospheric circulation patterns. In this sense, years with a marked negative SAM anomaly are associated with ice-covered sea conditions, whereas positive SAM phases are associated with ice-free sea conditions (Fig. 12). Other studies (Turner et al., 2016) point to a similar interaction between surface air temperature and SIE at API and recognized that the SIE's inter-annual variability is related to atmospheric modes. This supports our own observations in a way that the sea ice is important for regulation of surface air temperatures in the region.

In firn cores obtained from API, mean $\delta^{18}\text{O}$ and δD values show a decreasing trend with increasing height from sea level up to LCL (1130 m a.s.l.), which provides evidence for the altitudinal effect identified by Fernandoy et al. (2012). In addition, standard deviation of seasonal (monthly mean) δD and $\delta^{18}\text{O}$ values of firn cores from LCL is low and similar to that of the firn cores from lower altitudes. Despite the variations in isotopic composition with height, in all firn cores the $\delta\text{D} - \delta^{18}\text{O}$ co-isotopic relation is very similar to the LMWL obtained from precipitation samples at OH. This provides evidence of the uniformity of the fractionation conditions during the condensation process. Although a slight isotopic smoothing effect was distinguished between the cores (16% after one year of deposition), the distortions caused by post-depositional effects that may alter or homogenize the isotopic signal at this site, such as diffusion, can be considered as limited. The latter indication is well supported by the high accumulation rate in the region that does not allow a prolonged exposition of the freshly fallen snow to the atmosphere. Furthermore, the absence of significant infiltration and percolation associated with melting and refreezing events and the lack of a relationship between ice layers and the stable water isotope record implies that the formation of melt layers is not related to variations in the isotopic signal obtained from firn cores. Thus, this reassures that post-depositional processes in the LCL region are negligible in the time period analyzed and that ice layers likely developed by wind ablation on wind-scouring processes at the plateau. Although these observations are in agreement with the results obtained in this region by Fernandoy et al. (2012) and Aristarain et al. (1990), several studies (Fernandoy et al., 2012; Simões et al., 2004; Travassos and Simoes, 2004; Jiahong et al., 1998) have identified a significant amount of melt layers in firn cores, mainly from KGI and from the western side of the API at altitudes below 700 m a.s.l. The limited effect of post-depositional processes due to the high accumulation rates and to the ice layers reducing diffusion (Stichler et al., 2001), along with the high correlation between $d_{\text{excess}}^{\text{meteo}}$ and d_{excess} obtained from firn cores, confirm that the isotopic variations observed in firn core isotope records are mostly related to isotopic fractionation occurring during condensation and to rh and SST conditions in the vapor source regions.

4.2 Firn age model and accumulation rates

The stable water isotope signal obtained from firn cores shows no regularity in its seasonal behavior and lacks a clear annual oscillation pattern, possibly because of the strong maritime influence (Clark and Fritz, 1997). These two criteria prevent the development of an age model by conventional annual layer counting in the isotope record (Legrand and Mayewski, 1997). In this context, the d_{excess} parameter represents a robust time indicator, as it has shown to be principally dependent on rh and SST



conditions prevailing in the eastern Bellingshausen Sea where these variables are relatively stable (Jouzel et al., 2013). The high correlation coefficients (and high statistical significance) obtained for the relationship between d_{excess} and $d_{excess\ meteor}$, as shown in section 3.2.1, demonstrate that the method used to construct time series is effective in dating isotope records of firn cores from the northern API, even at a monthly resolution.

- 5 The most frequent d_{excess} values found in the firn cores (3‰ - 6‰) are in agreement with a strong coastal influence scenario as determined by Petit et al. (1991), implying that the d_{excess} relates to rh and SST of the humidity source and not to surface air temperature (Jouzel et al., 2013). Saigne and Legrand (1987), postulated that rh conditions prevailing at the sea surface have an important effect on the d_{excess} signal of precipitation below 2000 m a.s.l in the study region. The stable water isotope results, in combination with the meteorological records presented in this work, show that precipitation on LCL is highly correlated
10 with rh and SST conditions in the Bellingshausen Sea near the API.

The irrelevance of post-depositional effects along with the flat topography on LCL suggests that the estimate of accumulation rates from firn cores is representative of the amount of snow originally precipitated. Moreover, the slight smoothing of the isotope signal effect after deposition along with only small differences in the accumulation rate observed for the common time period of firn cores OH-9 and OH-10, demonstrates that our age model is reliable, as two different data sets yield similar
15 estimations for a common period. The results obtained allow to classify LCL as a high annual snow accumulation site (Table 4), closely following the estimations of other authors on King George Island dome (Bintanja, 1995; Zamoruyev, 1972; Jiahong et al., 1998) and on the API further south of LCL (Dalla Rosa, 2013; Goodwin, 2013; van Wessem et al., 2015), of around 2000 - 2500 kg m⁻² y⁻¹, but differs from the accumulation rate obtained by Simões et al. (2004) and Jiankang et al. (1994) on King George Island dome (600 kg m⁻² y⁻¹). A seasonal bias of the accumulation was noted, with more favorable conditions for
20 accumulation (i.e. higher precipitation amount) during autumn resulting from more synoptic scale features approaching the API (Table 4).

4.3 Seasonal variability and disruption of atmospheric conditions

The depletion of $\delta^{18}\text{O}$ with increasing height (altitude effect) and the simultaneous increase in accumulation along the western side of API at LCL latitude can be explained with the help of an orographic precipitation model as proposed by Martin and
25 Peel (1978). This model states that moist air parcels from the Southern Ocean are forced to ascend and cool down when approaching the API due to the steep topography forming an orographic barrier to westerly winds. The depletion observed in $\delta^{18}\text{O}$ could reflect the strength of the fractionation process taking place within a short distance and in a low temperature environment (Fig. 15a). Therefore, the isotopic fractionation process occurring along the API and the direct linear relation between $\delta^{18}\text{O}$ and condensation temperature allow us to study the temperature behavior with respect to the altitude increase on
30 the basis of $\delta^{18}\text{O}$ variations (Craig, 1961). However, whereas MAM air temperatures show a clear decrease with increasing height (atmospheric instability of the lower troposphere), JJA air temperatures exhibit an inverse pattern (an increase) from sea level up to 350 m a.s.l (atmospheric stability). At higher altitudes, a decreasing temperature trend is observed (atmospheric instability). The break at 350 m a.s.l during JJA indicates the existence of a strong stratification within the lower troposphere



on the western side of the API. In addition, the variations in monthly mean lapse rates measured by radiosondes in BE throughout the year, provide evidence for the existence of a process that modifies the behavior of the lower troposphere, decreasing the lapse rate (between sea level and 850 hPa) during JJA and considerably increasing it during DJF (Fig. 16).

5 The close linear relationship identified between lapse rate magnitude and SIE indicates that SIE is an important factor for the development of these variations between May and September.

The phenomena previously described is likely linked to the development of an inversion layer in the lower troposphere on the western side of the API mainly during JJA, which in turn is related to a strong radiative imbalance. During JJA, solar radiation diminishes until it reaches a minimum at the winter solstice. The lack of solar radiation leads to considerable cooling that favors the formation of sea ice and in turn, causes differential cooling between the sea ice surface and the air above it. As the
10 sea ice surface cools faster than the air above it, a near-surface altitudinal pattern of increasing temperature develops where local atmospheric stability prevails. The layer of atmospheric stability extends from sea level up to at least 350 m a.s.l, where it turns into an atmospheric instability regime. Both regimes together favor the decrease of the overall lapse rate, as temperature first increases and then decreases with height. Conversely, no inversion layer is formed during DJF due to the absence of sea ice and hence, atmospheric instability prevails, which is related to high lapse rates (Fig. 15b and 15c).

15 The existence of an inversion layer during the months with sea ice coverage might explain the low oscillation of monthly mean temperatures estimated at LCL compared to monthly mean air temperatures at BE (OH). The inverse relation between SAM index and SIE also seems to play an important role, as SAM positive phases enhance the transport of warm and moist air towards the western side of the API, thus inhibiting the formation of sea ice. This has a direct impact on the lapse rate as the development of an inversion layer is hindered and therefore air temperatures on LCL are regulated. The interaction between
20 SAM and SIE plays a key role as sea-ice-covered conditions temper the maritime system, favoring continental-like conditions and reducing annual mean air temperature, implying a higher temperature amplitude in BE and OH throughout the year.

The temperature time series estimated from the stable water isotope record ($\delta^{18}\text{O}$ and d_{excess}) from LCL firn cores exhibits a periodic (biannual) pattern, which can be linked to a similar periodical behavior observed in SAM index and in SIE. The relatively constant temperatures observed during MAM, JJA and SON in years with a positive SAM phase provide evidence
25 that during these seasons condensation is taking place at similar temperatures. Under such conditions (positive SAM), the low variations in the lapse rate throughout the year, along with the low thermal oscillation in BE (OH) explain the presence of a constant condensation temperature, which does not differ much from air temperature during DJF. Conversely, the stronger annual temperature oscillation observed on LCL during negative SAM phases indicates marked variations in condensation temperature throughout the year.

30 Finally, the proposed inversion layer model (Fig. 16) explains the seasonal variations observed in the $\delta^{18}\text{O} - T$ relationship of precipitation samples from OH. The distortion of the direct relation between condensation temperature and surface air temperature by an inversion layer makes it necessary to differentiate $\delta^{18}\text{O} - T$ relationship according to the lapse rate evolution throughout the year. In this context, MAM and SON were identified as transitional periods in the formation of the inversion layer, mainly because of the sea-ice formation and retreat during these seasons. The seasonal adjustment considered to estimate



LCL temperatures must be applied mainly, because the sea–ice cover varies inter–annually in its duration and extension, which in turn produces the inter–annually variable inversion layer. The proposed model for the coastal region on the western side of the API at OH latitude, is consistent with the observations of Yaorong et al. (2003) on KGI (South Shetland Islands), through which the development of several inversion layers that extend beyond 400 m a.s.l.

5 5 Conclusions

In this study, we examined one of the most complete records of recent precipitation from the northern API, with a total of 210 single precipitation events and more than 60 m of firn cores. The firn cores retrieved in this work include the accumulation at the northwestern API region between 2006 and 2014 from. Precipitation and firn stable water isotope compositions have been compared to different meteorological data sets to determine their representativeness as climate proxy for the region.

- 10 The results of our study reveal significant seasonal changes in the $\delta^{18}\text{O} - T$ relationship throughout the year. For autumn and spring a $\delta^{18}\text{O} - T$ ratio of $0.69\text{‰ } ^\circ\text{C}^{-1}$ ($r=0.74$) was found to be most representative, whereas for winter and summer the $\delta^{18}\text{O} - T$ ratio appears to be highly dependent on SIE conditions. The apparent moisture source for air parcels precipitating at the northern API is mainly located in the Bellingshausen Sea and in the southern Pacific Ocean. The transport of water vapor along these oceanic and coastal pathways exerts a strong impact on the d_{excess} signal of precipitation. The comparison between the
- 15 d_{excess} signal from the moisture source and the d_{excess} signal from firn cores has proved to be a successful method for dating firn cores from the northern API, delivering a seven–year isotopic time series in high temporal resolution for LCL.

- Based on our dating method we could define LCL as a high snow accumulation site, with a mean annual accumulation rate of $1770 \text{ kg m}^{-2} \text{ y}^{-1}$ for the period 2006–2014. However, accumulation is highly variable from year to year, with a maximum and minimum of 2470 kg m^{-2} (in 2008) and 1060 kg m^{-2} (in 2010), respectively. In addition, we identified the presence of a strong
- 20 orographic precipitation effect along the western side of the API reflected by an accumulation increase with altitude ($1500 \text{ kg m}^{-2} \text{ y}^{-1} \text{ km}^{-1}$), as well as by the isotopic depletion of precipitation from sea level up to LCL (-2.4‰ km^{-1} for autumn) and from the coast line up to the ice divide (-0.08‰ km^{-1}).

- The maritime regime present on the western side of the API has a strong control on air temperatures, observed as restricted summer/winter oscillation, and is reflected in a poor seasonality of the $\delta^{18}\text{O}$ and δD profiles in firn cores. Recent climatic
- 25 conditions can be reconstructed from $\delta^{18}\text{O}$ time series obtained from LCL firn cores only when considering an inversion layer model during winter season. The strength of the inversion layer likely depends on SIE and SAM index values. Taking into account the effect of the inversion layer on the isotope–temperature relationship, we observe a slight cooling trend of mean annual air temperature at LCL with an approximate rate of $-0.33^\circ\text{C y}^{-1}$ for the period sampled by the examined firn cores (2009–2014). This finding is in line with evidence from stacked meteorological record of the nearby research stations as
- 30 determined by Turner et al. (2016).

Our results demonstrate that the stable water isotope composition of firn cores retrieved from LCL is capable of reproducing the meteorological signal present in this region, validating it as a valuable proxy for paleo–climate reconstructions in the



northern API region. Environmental (atmosphere and ocean) and glaciological conditions present at LCL, a ~350 m thick ice cap, together with an almost undisturbed isotopic record are optimal prerequisites for the preservation of a climate proxy record with a high temporal resolution. Consequently, LCL is a suitable site for recovering a medium–depth ice core to investigate climate variations during the last centuries in the northern API region.

5 6 Acknowledgements

The present work was funded by the FONDECYT project 11121551 and supported by the Chilean Antarctic Institute (INACH), the Chilean Air Force and Army logistic facilities. We want to show our gratitude to the Universidad Nacional Andres Bello for supporting this study. We also greatly thank our colleagues, who made field work conditions less severe, especially to Daniel Rutllant for his support on the logistic and field safety. Finally, we would like to thank all people involved on the laboratory work, especially to Ivonne Quintanilla, who carried out the sample processing at UNAB and to Dr. Johannes Freitag, for his support with the X-Ray tomography processing at AWI.

References

- Abram, N. J., Mulvaney, R., Wolff, E. W., Triest, J., Kipfstuhl, S., Trusel, L. D., Vimeux, F., Fleet, L., and Arrowsmith, C.: Acceleration of snow melt in an Antarctic Peninsula ice core during the twentieth century, *Nature Geosci*, 6, 404-411, doi: 10.1038/ngeo1787, 2013.
- 15 Annan, A. P., and Davis, J. L.: Impulse radar sounding in permafrost, *Radio Science*, 11, 383-394, doi: 10.1029/RS011i004p00383, 1976.
- Arcone, S. A.: *Glaciers and Ice Sheets*, in: *Ground Penetrating Radar Theory and Applications*, First edition ed., edited by: Jol, H. M., Elsevier Science, Amsterdam, 361-392, 2009.
- 20 Aristarain, A., Jouzel, J., and Pourchet, M.: Past Antarctic Peninsula climate (1850-1980) deduced from an ice core isotope record, *Climatic Change*, 9, 69-89, 1986.
- Aristarain, A., Jouzel, J., and Lorius, C.: A 400 Year Isotope record of the Antarctic Peninsula climate, *Geophys. Res. Lett.*, 17, 2369-2372, doi: 10.1029/GL017i013p02369, 1990.
- Bintanja, R.: The local surface energy balance of the Ecology Glacier, King George Island, Antarctica: measurements and modelling, *Antarctic Science*, 7, 315-325, doi: 10.1017/S0954102095000435, 1995.
- 25 Bromwich, D. H., Nicolas, J. P., Monaghan, A. J., Lazzara, M. A., Keller, L. M., Weidner, G. A., and Wilson, A. B.: Central West Antarctica among the most rapidly warming regions on Earth, *Nature Geosci*, 6, 139-145, doi: 10.1038/ngeo1671, 2013.
- Cárdenas, C., Johnson, E., Fernandoy, F., Meyer, H., Cereceda, F., and Vidal, V.: Preliminary results of the superficial and sub-glacier topography survey using Radio Echo Sounding at the La Claveré Plateau, Antarctic Peninsula, SCAR Open Science Conference, Auckland, New Zealand, 1-3 September, 2014.
- 30 Carrasco, J. F.: Decadal Changes in the Near-Surface Air Temperature in the Western Side of the Antarctic Peninsula, *Atmospheric and Climate Sciences*, 03, 7, doi: 10.4236/acs.2013.33029, 2013.
- Clark, I., and Fritz, P.: *Environmental Isotopes in Hydrogeology*, edited by: Stein, J., and Starkweather, A., Lewis, Boca Raton, New York, 311 pp., 1997.
- 35 Craig, H.: Isotopic variations in meteoric waters, *Science*, 133, 1702-1703, doi: 10.1126/science.133.3465.1702, 1961.
- Dalla Rosa, J.: Variabilidade da taxa de acumulação de neve no Platô Detroit, Península Antártica, M.S. thesis, Instituto de Geociências, Universidade Federal do Rio Grande do Sul, Porto Alegre, 98 pp., 2013.
- Daniels, D. J.: *Ground penetrating radar*, 2nd ed., IET Radar, Sonar, Navigation and Avionics, 15, The Institution of Engineering and Technology, Herts, United Kingdom, 2007.



- Dierssen, H. M., Smith, R. C., and Vernet, M.: Glacial meltwater dynamics in coastal waters west of the Antarctic peninsula, *Proceedings of the National Academy of Sciences*, 99, 1790-1795, doi: 10.1073/pnas.032206999, 2002.
- Draxler, R. R., and Hess, G. D.: An Overview of the HYSPLIT-4 modelling system for trajectories, dispersion and deposition, *Aust. Meteorol. Mag.*, 47, 295-308, 1998.
- 5 Dutrieux, P., De Rydt, J., Jenkins, A., Holland, P. R., Ha, H. K., Lee, S. H., Steig, E. J., Ding, Q., Abrahamsen, E. P., and Schröder, M.: Strong Sensitivity of Pine Island Ice-Shelf Melting to Climatic Variability, *Science*, 343, 174-178, doi: 10.1126/science.1244341, 2014.
- Falk, U., and Sala, H.: Winter melt conditions of the inland ice cap on King George Island, Antarctic Peninsula, *Erkunde*, 69, 341-363, doi: 10.3112/erdkunde.2015.04.04, 2015.
- 10 Fernandoy, F., Meyer, H., and Tonelli, M.: Stable water isotopes of precipitation and firn cores from the northern Antarctic Peninsula region as a proxy for climate reconstruction, *The Cryosphere*, 6, 313-330, doi: 10.5194/tc-6-313-2012, 2012.
- Fyfe, J. C., and Saenko, O. A.: Human-Induced Change in the Antarctic Circumpolar Current, *Journal of Climate*, 18, 3068-3073, doi: 10.1175/JCLI3447.1, 2005.
- Fyfe, J. C., Saenko, O. A., Zickfeld, K., Eby, M., and Weaver, A. J.: The Role of Poleward-Intensifying Winds on Southern Ocean Warming, *Journal of Climate*, 20, 5391-5400, doi: 10.1175/2007JCLI1764.1, 2007.
- 15 Gille, S. T.: Decadal-Scale Temperature Trends in the Southern Hemisphere Ocean, *Journal of Climate*, 21, 4749-4765, doi: 10.1175/2008JCLI2131.1, 2008.
- Goodwin, B. P.: Recent Environmental Changes on the Antarctic Peninsula as Recorded in an ice core from the Bruce Plateau, Ph.D. thesis, Graduate Program in Atmospheric Science, Ohio State University, 247 pp., 2013.
- 20 Goodwin, B. P., Mosley-Thompson, E., Wilson, A. B., Porter, S. E., and Sierra-Hernandez, M. R.: Accumulation Variability in the Antarctic Peninsula: The Role of Large-Scale Atmospheric Oscillations and Their Interactions, *Journal of Climate*, 29, 2579-2596, doi: 10.1175/JCLI-D-15-0354.1, 2015.
- Harig, C., and Simons, F. J.: Accelerated West Antarctic ice mass loss continues to outpace East Antarctic gains, *Earth and Planetary Science Letters*, 415, 134-141, doi: 10.1016/j.epsl.2015.01.029, 2015.
- 25 Jiahong, W., Jiancheng, K., Jiankang, H., Zichu, X., Leibao, L., and Dali, W.: Glaciological studies on the King George Island ice cap, South Shetland Islands, Antarctica, *Annals of Glaciology*, 27, 105-109, doi: 10.3198/1998AoG27-1-105-109, 1998.
- Jiankang, H., Jiancheng, K., Jiahong, W., Lluberas, A., and Rodriguez, F.: General characteristics in stratigraphy and density variation for ice cores from Collins Ice Cap, King George Island, Antarctica, *Antarctic Research*, 6, 40-46, 1994.
- Jouzel, J., Delaygue, G., Landais, A., Masson-Delmotte, V., Risi, C., and Vimeux, F.: Water isotopes as tools to document oceanic sources of precipitation, *Water Resources Research*, 49, 7469-7486, doi: 10.1002/2013WR013508, 2013.
- 30 Kanamitsu, M.: Description of the NMC Global Data Assimilation and Forecast System, *Weath. Forecast.*, 4, 335-342, doi: 10.1175/1520-0434(1989)004<0335:DOTNGD>2.0.CO;2, 1989.
- Kuipers Munneke, P., Picard, G., van den Broeke, M. R., Lenaerts, J. T. M., and van Meijgaard, E.: Insignificant change in Antarctic snowmelt volume since 1979, *Geophysical Research Letters*, 39, doi: 10.1029/2011GL050207, 2012.
- 35 Legrand, M., and Mayewski, P.: Glaciochemistry of polar ice cores: A review, *Rev. Geophys.*, 35, 219-243, doi: 10.1029/96RG03527, 1997.
- Linow, S., Hörhold, M. W., and Freitag, J.: Grain-size evolution of polar firn: a new empirical grain growth parameterization based on X-ray microcomputer tomography measurements, *Journal of Glaciology*, 58, 1245-1252, doi: 10.3189/2012JoG11J256, 2012.
- 40 Marshall, G. J.: Trends in the Southern Annular Mode from observations and Reanalyses, *J. Climate*, 16, 4134-4143, doi: 10.1175/1520-0442(2003)016<4134:TITSAM>2.0.CO;2, 2003.
- Marshall, G. J., Orr, A., van Lipzig, N. P. M., and King, J. C.: The Impact of a Changing Southern Hemisphere Annular Mode on Antarctic Peninsula Summer Temperatures, *J. Climate*, 19, 5388-5404, doi: 10.1175%2FJCLI3844.1, 2006.
- Marshall, G. J.: Half-century seasonal relationships between the Southern Annular Mode and Antarctic temperatures, *Int. J. Climatol.*, 27, 373-383, doi: 10.1002/Joc.1407, 2007.
- 45 Martin, P. J., and Peel, D. A.: The Spatial Distribution of 10 m Temperatures in the Antarctic Peninsula, *Journal of Glaciology*, 20, 311-317, doi: 10.3198/1978JoG20-83-311-317, 1978.
- Masson-Delmotte, V., Hou, S., Ekaykin, A., Jouzel, J., Aristarain, A., Bernardo, R. T., Bromwich, D., Cattani, O., Delmotte, M., Falourd, S., Frezzotti, M., Gallée, H., Genoni, L., Isaksson, E., Landais, A., Helsen, M. M., Hoffmann, G., Lopez, J.,
- 50 Morgan, V., Motoyama, H., Noone, D., Oerter, H., Petit, J. R., Royer, A., Uemura, R., Schmidt, G. A., Schlosser, E., Simoes,



- J. C., Steig, E. J., Stenni, B., Stievenard, M., van den Broeke, M. R., van de Wal, R. S. W., van de Berg, W. J., Vimeux, F., and White, J. W. C.: A Review of Antarctic Surface Snow Isotopic Composition: Observations, Atmospheric Circulation, and Isotopic Modeling, *J. Climate*, 21, 3359-3387, doi: 10.1175%2F2007JCLI2139.1, 2008.
- 5 Meredith, M., and King, J. C.: Rapid climate change in the ocean west of the Antarctic Peninsula during the second half of the 20th century, *Geophys. Res. Lett.*, 32, 1 - 5, doi: 10.1029/2005GL024042, 2005.
- Meredith, M. P., Stammerjohn, S. E., Venables, H. J., Ducklow, H. W., Martinson, D. G., Iannuzzi, R. A., Leng, M. J., van Wessem, J. M., Reijmer, C. H., and Barrand, N. E.: Changing distributions of sea ice melt and meteoric water west of the Antarctic Peninsula, *Deep Sea Research Part II: Topical Studies in Oceanography*, doi: 10.1016/j.dsr2.2016.04.019, 2016.
- 10 Meyer, H., Schönicke, L., Wand, U., Hubberten, H. W., and Friedrichsen, H.: Isotope Studies of Hydrogen and Oxygen in Ground Ice - Experiences with the Equilibration Technique, *Isot. Environ. Health S.*, 36, 133 - 149, doi: 10.1080/10256010008032939, 2000.
- Moser, H., and Stichler, W.: Environmental isotopes in ice and snow, in: *Handbook of environmental isotope geochemistry*, edited by: Fritz, P., and Fontes, J. C., Elsevier, New York, 141-178, 1980.
- Peel, D. A., Mulvaney, R., and Davison, B. M.: Stable-Isotope/Air-Temperature relationship in ice cores from Dolleman Island and the Palmer Land Plateau, Antarctic Peninsula, *Ann. Glaciol.*, 10, 130-136, doi: 10.3198/1988AoG10-130-136, 1988.
- 15 Petit, J. R., White, J. W. C., Young, N. W., Jouzel, J., and Korotkevich, Y. S.: Deuterium Excess in Recent Antarctic Snow, *J. Geophys. Res-Atmos.*, 96, 5113-5122, doi: 10.1029/90JD02232, 1991.
- Pritchard, H. D., and Vaughan, D. G.: Widespread acceleration of tidewater glaciers on the Antarctic Peninsula, *J. Geophys. Res.*, 112, F03S29, doi: 10.1029/2006jf000597, 2007.
- 20 Pritchard, H. D., Ligtenberg, S. R. M., Fricker, H. A., Vaughan, D. G., van den Broeke, M. R., and Padman, L.: Antarctic ice-sheet loss driven by basal melting of ice shelves, *Nature*, 484, 502-505, doi: 10.1038/nature10968, 2012.
- Rayner, N. A., Parker, D. E., Horton, E. B., Folland, C. K., Alexander, L. V., Rowell, D. P., Kent, E. C., and Kaplan, A.: Global analyses of sea surface temperature, sea ice, and night marine air temperature since the late nineteenth century, *J. Geophys. Res-Atmos.*, 108, 4407, doi: 10.1029/2002jd002670, 2003.
- 25 Rignot, E., Casassa, G., Gogineni, S., Kanagaratnam, P., Krabill, W., Pritchard, H., Rivera, A., Thomas, R., Turner, J., and Vaughan, D.: Recent ice loss from the Fleming and other glaciers, Wordie Bay, West Antarctic Peninsula, *Geophys. Res. Lett.*, 32, L07502, doi: 10.1029/2004GL021947, 2005.
- Rozanski, K., Araguás-Araguás, L., and Gonfiantini, R.: Isotopic Patterns in Modern Global Precipitation, in: *Climate Change in Continental Isotopic Records*, edited by: Swart, P. K., Lohman, K. C., McKenzie, J., and Savin, S., American Geophysical Union, Washington, USA, 1993.
- 30 Saigne, C., and Legrand, M.: Measurements of methanesulphonic acid in Antarctic ice, *Nature*, 330, 240-242, doi: 10.1038/330240a0, 1987.
- Seehaus, T., Marinsek, S., Helm, V., Skvarca, P., and Braun, M.: Changes in ice dynamics, elevation and mass discharge of Dinsmoor–Bombardier–Edgeworth glacier system, Antarctic Peninsula, *Earth and Planetary Science Letters*, 427, 125-135, doi: 10.1016/j.epsl.2015.06.047, 2015.
- 35 Shepherd, A., Ivins, E. R., A, G., Barletta, V. R., Bentley, M. J., Bettadpur, S., Briggs, K. H., Bromwich, D. H., Forsberg, R., Galin, N., Horwath, M., Jacobs, S., Joughin, I., King, M. A., Lenaerts, J. T. M., Li, J., Ligtenberg, S. R. M., Luckman, A., Luthcke, S. B., McMillan, M., Meister, R., Milne, G., Mouginot, J., Muir, A., Nicolas, J. P., Paden, J., Payne, A. J., Pritchard, H., Rignot, E., Rott, H., Sørensen, L. S., Scambos, T. A., Scheuchl, B., Schrama, E. J. O., Smith, B., Sundal, A. V., van Angelen, J. H., van de Berg, W. J., van den Broeke, M. R., Vaughan, D. G., Velicogna, I., Wahr, J., Whitehouse, P. L., Wingham, D. J., Yi, D., Young, D., and Zwally, H. J.: A Reconciled Estimate of Ice-Sheet Mass Balance, *Science*, 338, 1183-1189, doi: 10.1126/science.1228102, 2012.
- Sigmond, M., Reader, M. C., Fyfe, J. C., and Gillett, N. P.: Drivers of past and future Southern Ocean change: Stratospheric ozone versus greenhouse gas impacts, *Geophysical Research Letters*, 38, doi: 10.1029/2011GL047120, 2011.
- 45 Simões, J., Ferron, F., Bernardo, R., Aristarain, A., Stievenard, M., Pourchet, M., and Delmas, R.: Ice core study from the King George Island, South Shetlands, Antarctica., *Pesquisa Antártica Brasileira*, 4, 9-23, 2004.
- Sinclair, K. E., Bertler, N. A. N., Trompeter, W. J., and Baisden, W. T.: Seasonality of Air-mass Pathways to Coastal Antarctica: Ramifications for Interpreting High-Resolution Ice Core Records, *Journal of Climate*, 26, 2065-2076, doi: 10.1175/JCLI-D-12-00167.1, 2012.



- Spikes, V. B., Hamilton, G. S., Arcone, S. A., Kaspari, S., and Mayewski, P. A.: Variability in accumulation rates from GPR profiling on the West Antarctic plateau, *Annals of Glaciology*, 39, 238-244, doi: 10.3189/172756404781814393, 2004.
- Stichler, W., Schotterer, U., Fröhlich, K., Ginot, P., Kull, C., Gäggeler, H., and Pouyaud, B.: Influence of sublimation on stable isotope records recovered from high-altitude glaciers in the tropical Andes, *J. Geophys. Res.*, 106, doi: 10.1029/2001jd900179, 2001.
- 5 Thomas, E. R., Marshall, G. J., and McConnell, J. R.: A doubling in snow accumulation in the western Antarctic Peninsula, *Geophys. Res. Lett.*, 35, 1-5, doi: 10.1029/2007GL032529, 2008.
- Thomas, E. R., and Bracegirdle, T. J.: Improving ice core interpretation using in situ and reanalysis data, *J. Geophys. Res.*, 114, D20116, doi: 10.1029/2009jd012263, 2009.
- 10 Thomas, E. R., Dennis, P. F., Bracegirdle, T. J., and Franzke, C.: Ice core evidence for significant 100-year regional warming on the Antarctic Peninsula, *Geophys. Res. Lett.*, 36, -, doi: 10.1029/2009gl040104, 2009.
- Thomas, E. R., and Bracegirdle, T. J.: Precipitation pathways for five new ice core sites in Ellsworth Land, West Antarctica, *Climate Dynamics*, 44, 2067-2078, doi: 10.1007/s00382-014-2213-6, 2015.
- Thompson, D. W. J., and Solomon, S.: Interpretation of Recent Southern Hemisphere Climate Change, *Science*, 296, 895-899, 10.1126/science.1069270, 2002.
- 15 Travassos, J., and Simoes, J.: High-resolution radar mapping of internal layers of a subpolar ice cap, King George Island, Antarctica, *Pesquisa Antártica Brasileira*, 4, 57-65, 2004.
- Trusel, L. D., Frey, K. E., and Das, S. B.: Antarctic surface melting dynamics: Enhanced perspectives from radar scatterometer data, *Journal of Geophysical Research: Earth Surface*, 117, doi: 10.1029/2011JF002126, 2012.
- 20 Turner, J., Colwell, S. R., Marshall, G. J., Lachlan-Cope, T. A., Carleton, A. M., Jones, P. D., Lagun, V., Reid, P. A., and Jagovkina, S.: The SCAR READER project: Toward a high-quality database of mean Antarctic meteorological observations, *J. Climate*, 17, 2890-2898, doi: 10.1175/1520-0442(2004)017<2890:TSRPTA>2.0.CO;2, 2004.
- Turner, J., Colwell, S. R., Marshall, G. J., Lachlan-Cope, T. A., Carleton, A. M., Jones, P. D., Lagun, V., Reid, P. A., and Jagovkina, S.: Antarctic climate change during the last 50 years, *Int. J. Climatol.*, 25, 279-294, doi: 10.1002/joc.1130, 2005.
- 25 Turner, J., Lu, H., White, I., King, J. C., Phillips, T., Hosking, J. S., Bracegirdle, T. J., Marshall, G. J., Mulvaney, R., and Deb, P.: Absence of 21st century warming on Antarctic Peninsula consistent with natural variability, *Nature*, 535, 411-415, doi: 10.1038/nature18645, 2016.
- Uemura, R., Matsui, Y., Yoshimura, K., Motoyama, H., and Yoshida, N.: Evidence of deuterium excess in water vapor as an indicator of ocean surface conditions, *J. Geophys. Res.*, 113, 1-10, doi: 10.1029/2008JD010209, 2008.
- 30 van Wessem, J. M., Reijmer, C. H., van de Berg, W. J., van den Broeke, M. R., Cook, A. J., van Ulft, L. H., and van Meijgaard, E.: Temperature and Wind Climate of the Antarctic Peninsula as Simulated by a High-Resolution Regional Atmospheric Climate Model, *Journal of Climate*, 28, 7306-7326, doi: 10.1175/JCLI-D-15-0060.1, 2015.
- Yaorong, H., Zhenhe, X., and Cong, X.: A Study on Snowstorm Weather in Coastal Area of Western Antarctic, *Marine Science Bulletin*, 5, 24-31, 2003.
- 35 Zamoruyev, V. V.: Results of glaciological observations at Bellingshausen station in 1968, *Trudy Sovetskoy Antarkticheskoy Ekspeditsii*, 55, 135-144, 1972.

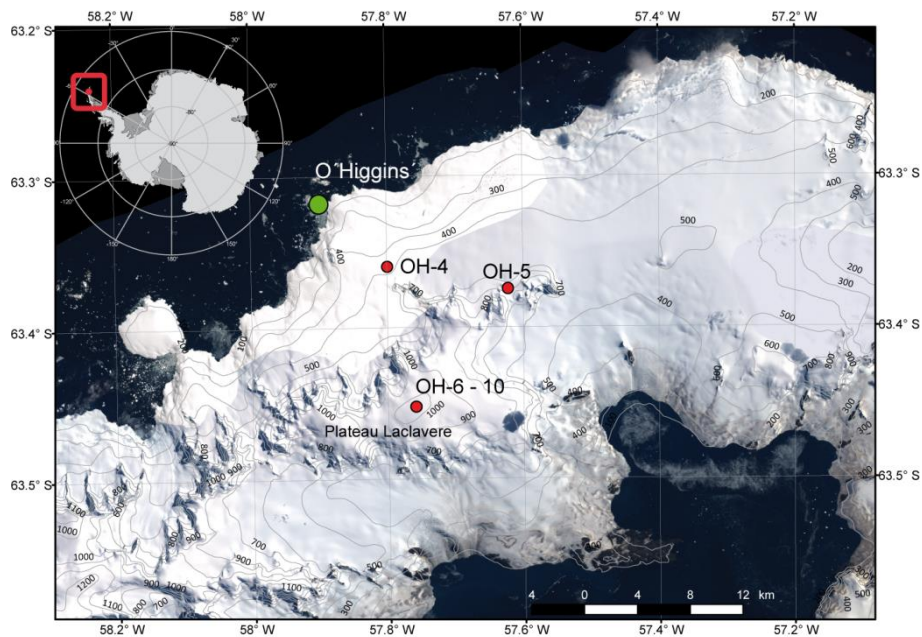


Figure 1: Investigation area and location of the firn cores presented in this work. The green point shows the Chilean Station O'Higgins (OH) at the west coast of the Antarctic Peninsula. Firn cores retrieved between 2008 and 2015 are shown by red dots.

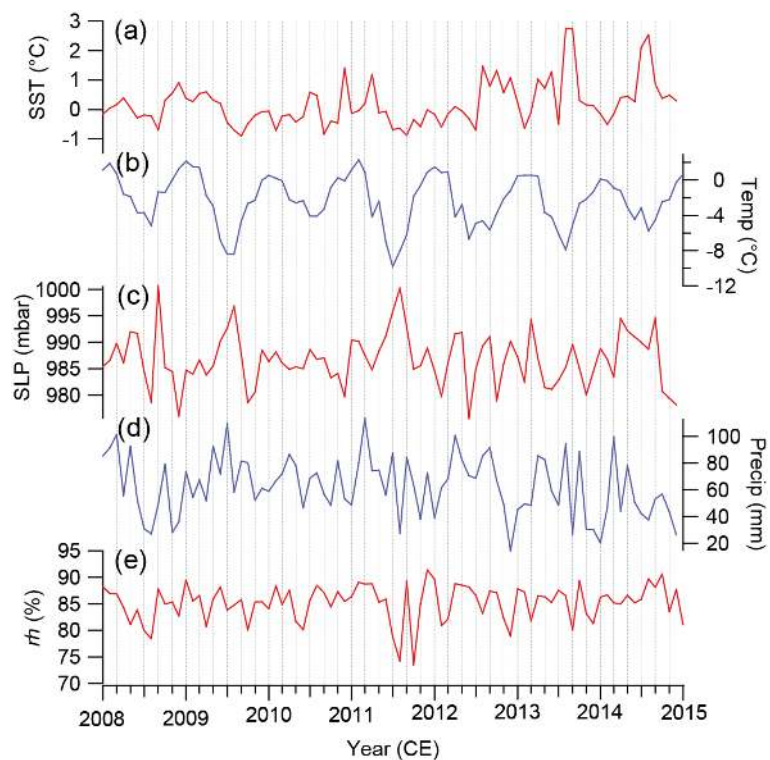


Figure 2: Meteorological data sets used in this study, (a) Sea surface temperature (SST), (b) Air temperature (Temp), (c) Sea level pressure (SLP) and (d) Precipitation amount (Precip) from Bellingshausen Station (BE) on King George Island and (e) Relative humidity (rh) from the Southern Ocean surrounding the northern Antarctic Peninsula (API) region

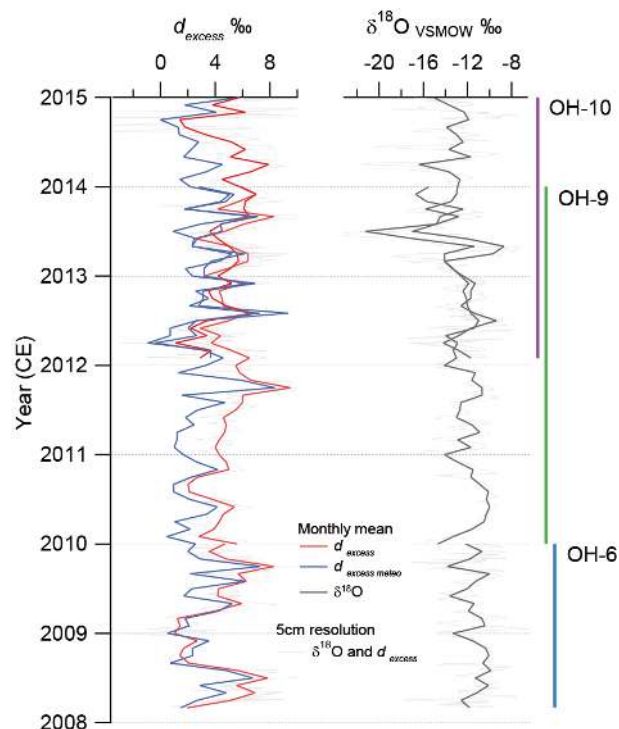


Figure 3: Time series for firn cores OH-6 (light blue line right), OH-9 (green light right) and OH-10 (purple line right) derived for $\delta^{18}\text{O}$ (black line right) and d_{excess} (red line left) records using a theoretical d_{excess} ($d_{\text{excess meteo}}$) value (blue line left). The $d_{\text{excess meteo}}$ is calculated from Sea surface temperature (SST) and Relative Humidity (rh) according to Uemura et al. (2008).

5

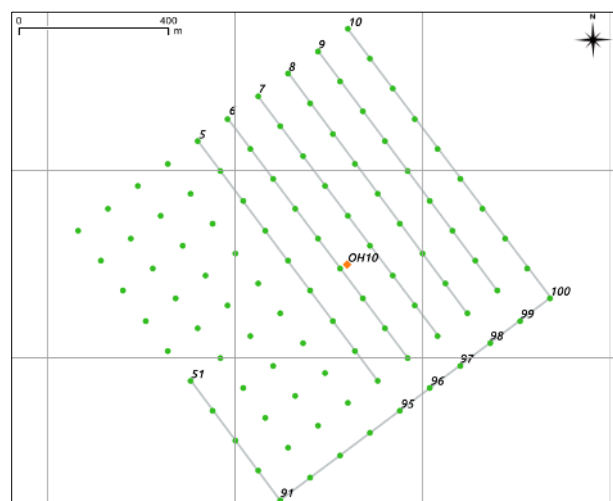


Figure 4: Grid designed to carry out GPR measurements in the area around the drill site of OH-10. Green dots denote marks of 100 m span between them. Grey lines show the sections that were covered by the GPR measurements. Continuous grey lines indicate the completed profiles. Other proposed lines were not possible to be completed due to adverse meteorological conditions.

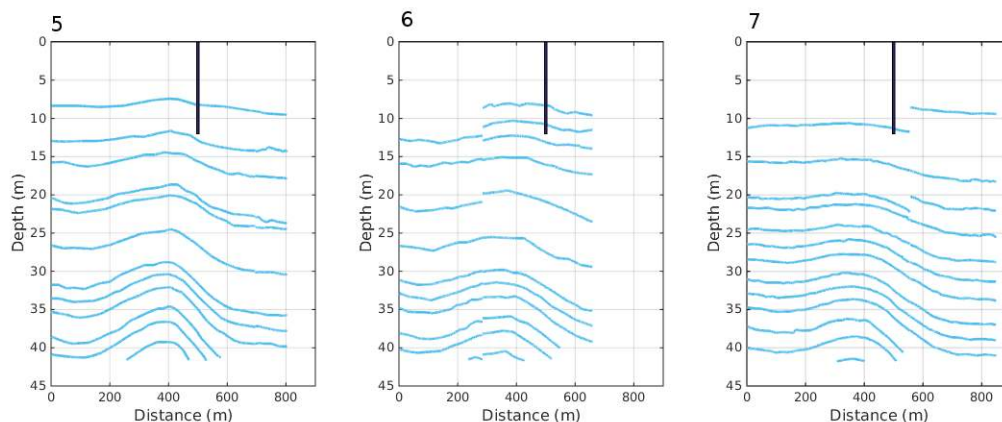


Figure 5: Layer interpretation (light blue lines) of radar imaging collected near the extracted the drill site of firn core OH-10. From left to right: 5, 6 and 7 mark the starting point of the measurement (see Fig. 4 for location). The black bars indicate the depth of the firn core retrieved (OH-10).

5

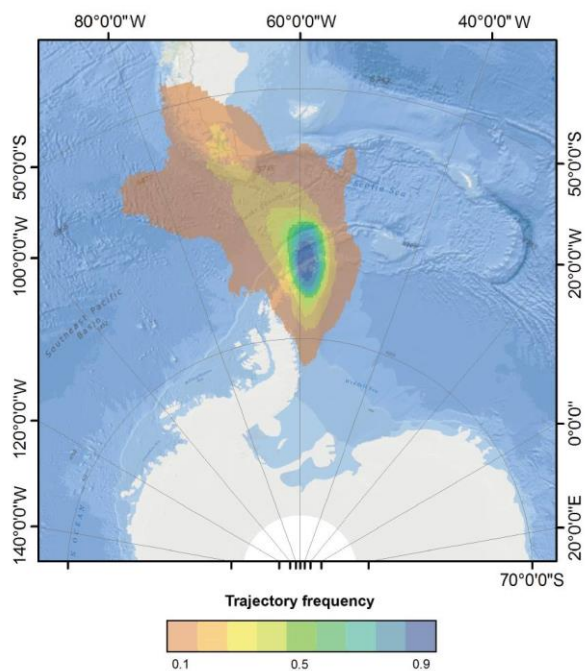
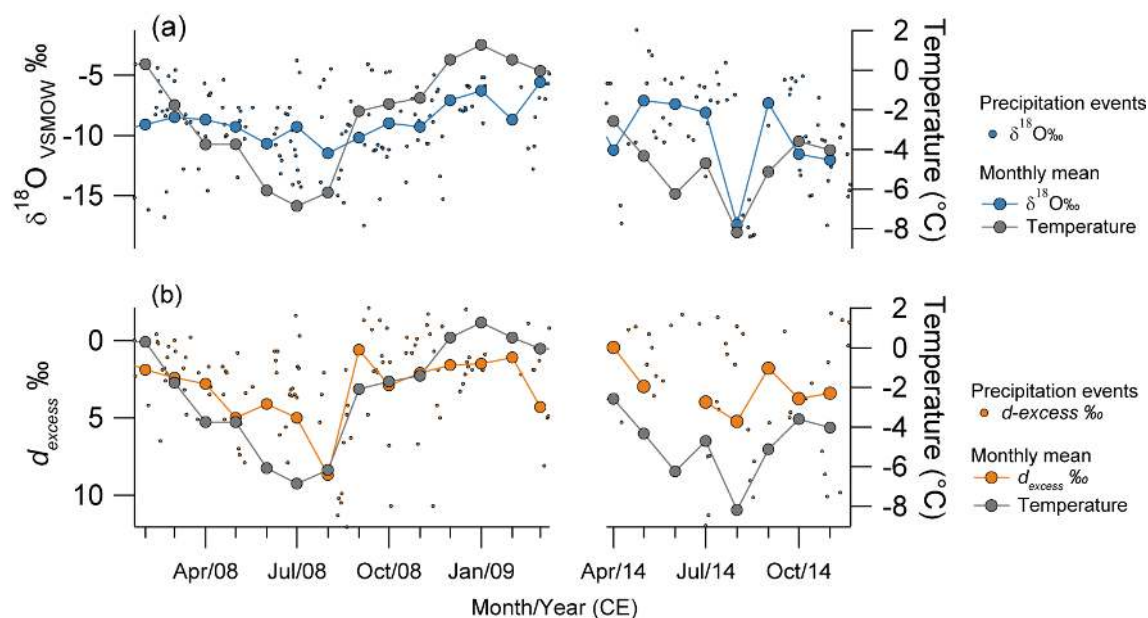
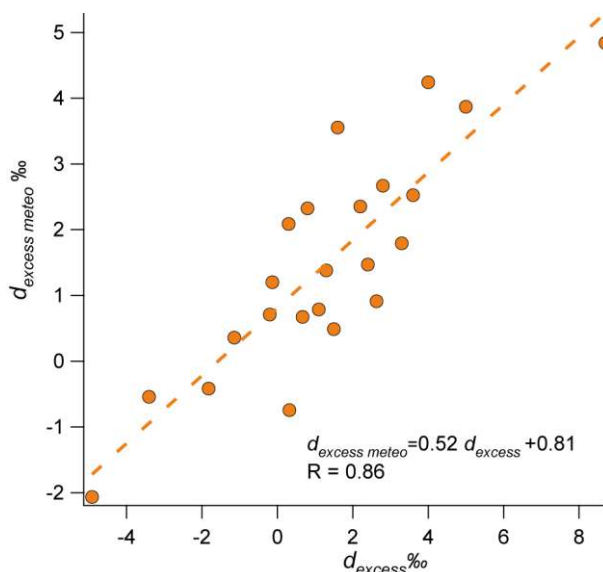


Figure 6: Frequency distribution map of the main transport paths of air masses approaching the northern Antarctic Peninsula (API). Translucent red colours represent the lowest frequency and blue colours the higher frequency. In general most of the air masses arriving at the API are coming from the Bellingshausen Sea and the South Pacific Ocean.

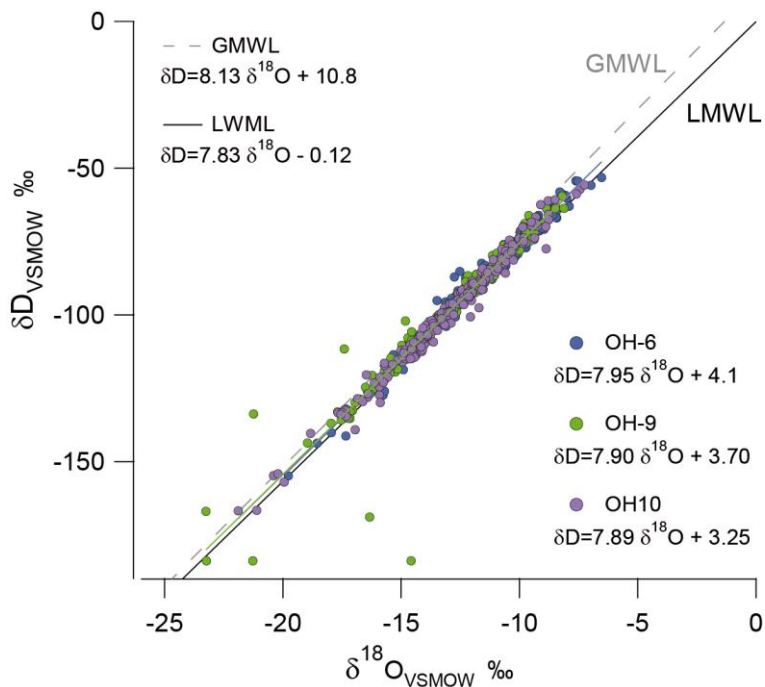
10



5 **Figure 7:** Stable water isotope composition of precipitation events and air temperature at O'Higgins Station. (a) shows the $\delta^{18}\text{O}$ composition of precipitation of single daily events (small solid blue dots) and monthly means (big solid blue dots and line) and (b) deuterium excess (d_{excess}) of single daily events (small orange dots) and monthly means (big orange dots and line). In both (a) and (b) monthly mean air temperature is also shown (grey solid dots and line).



10 **Figure 8:** Correlation between monthly mean deuterium excess values (d_{excess}) from firn cores and theoretical deuterium excess values calculated from meteorological parameters of the moisture source region ($d_{\text{excess meteo}}$) according to Uemura et al. (2008).



5 **Figure 9:** Co-isotopic relationship of firn cores OH-6 (solid blue dots), OH-9 (solid green dots) and OH-10 (solid purple dots). All slopes and intercepts are very close to each other as well as to the global and local meteoric water line (GMWL – grey dashed line, and LMWL – black solid line, respectively). Stable water isotope analysis for each firn core was made at 5cm resolution, representing 630 samples in total.

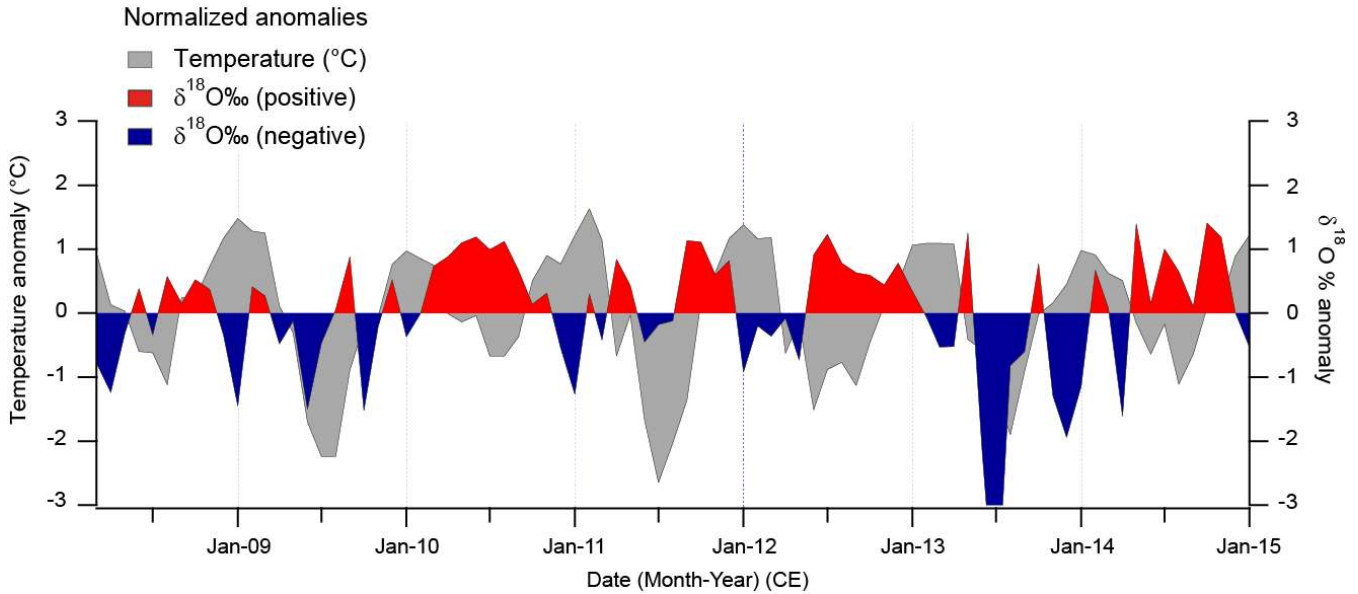


Figure 10: Standardized anomalies for air temperatures (solid grey colours) registered at Bellingshausen Station (BE) on King George Island and a composite $\delta^{18}\text{O}$ time series derived from firm cores OH-6, OH-9 and OH-10 from Laclavere Plateau (LCL). Both time series were detrended prior to constructing the time series of anomalies.

5

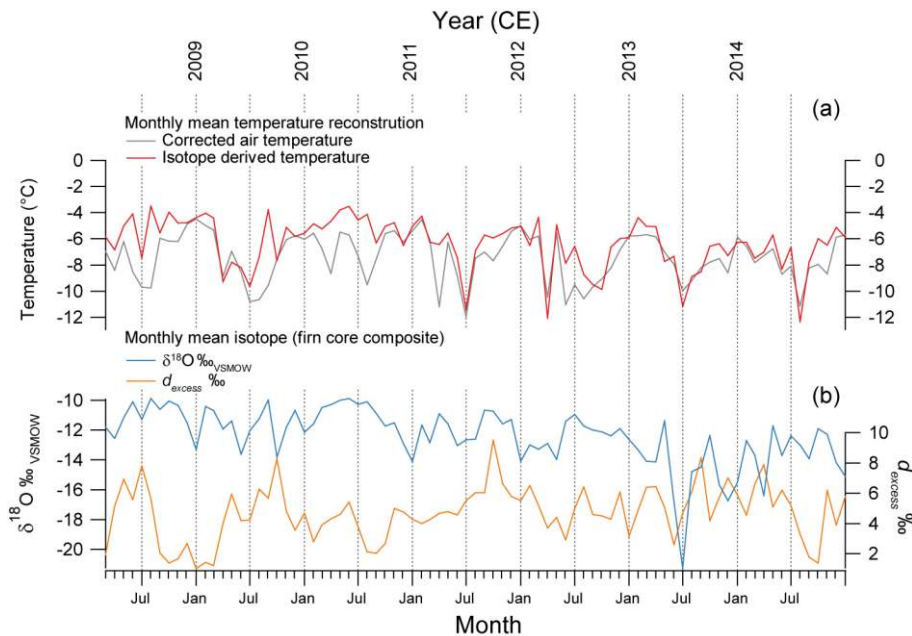
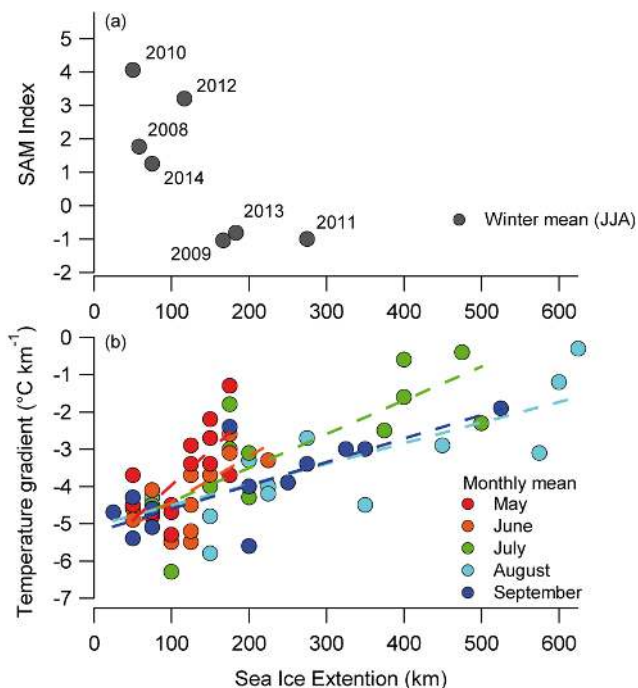
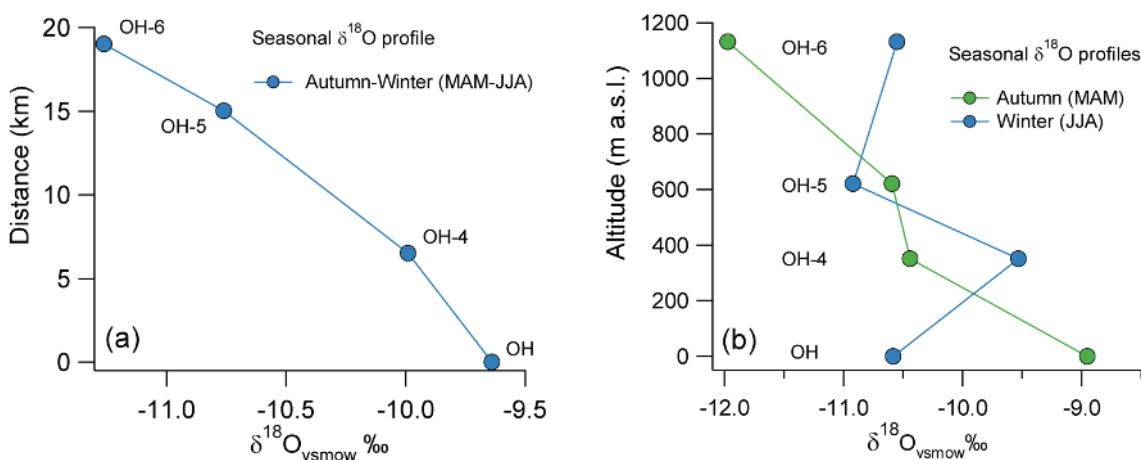


Figure 11: (a) Monthly mean air temperature reconstruction for LCL between March 2008 and January 2015 based on air temperature corrected by a seasonal factor and altitudinal gradient (grey line) and based on a $\delta^{18}\text{O}$ composite time series derived from firm cores from LCL corrected by a seasonal factor (red line), respectively. (b) $\delta^{18}\text{O}$ and d_{excess} monthly mean composite time series of LCL firm cores used for the temperature reconstruction of the upper panel.

10



5 **Figure 12:** Sea ice extent (SIE) from O’Higgins Station (OH) and its relationship to (a) the Southern Annular Mode and (b) to the temperature gradient between sea level and 1100 m a.s.l. at the Laclavere Plateau (LCL). SIE exhibits a negative relationship to the Southern Annular Mode between 2008 and 2014. The relationship to the temperature gradient is positive. A decreasing seasonal pattern of the temperature gradient can be observed from May to September (1979 – 1996).



10 **Figure 13:** δ¹⁸O profile with relation to (a) the distance from the coast at O’Higgins Station (OH) and at different points on the west flank of the API (6.5 km (OH-4), 15 km (OH-5) and 19 km (OH-6)) and (b) altitude at 350 m (OH-4), 620 m (OH-5) and 1130 m a.s.l. (OH-6) during autumn (MAM) (green solid dots) and winter (JJA) (blue solid dots).

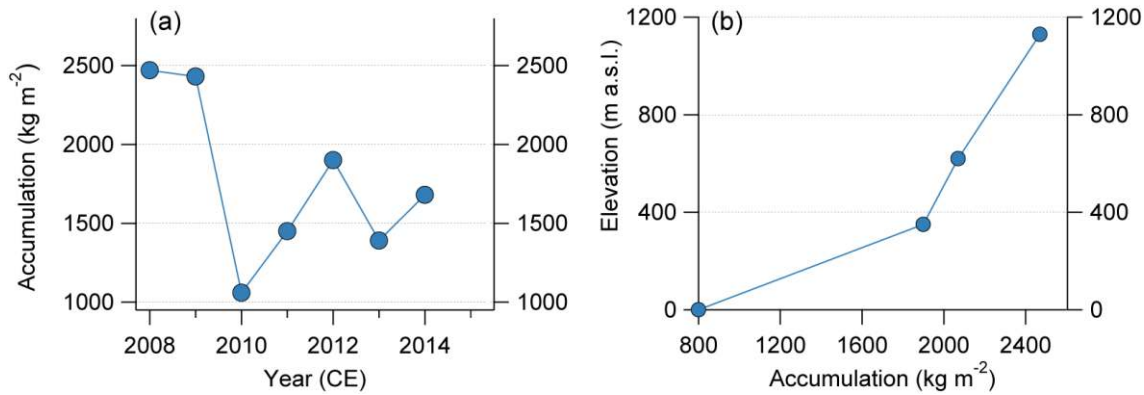


Figure 14: (a) Accumulation rates for Plateau Laclavere during 2008 – 2014 estimated from the stable water isotope composition of firn cores OH-6, OH-9 and OH-10 and their respective density profiles. (b) Accumulation variability for the west flank of the northern Antarctic Peninsula from the coast to Laclavere Plateau. Accumulation rates were derived from precipitation at O’Higgins Station at sea level and firn cores (OH-4, OH-5 and OH-6) for higher altitudes.

5

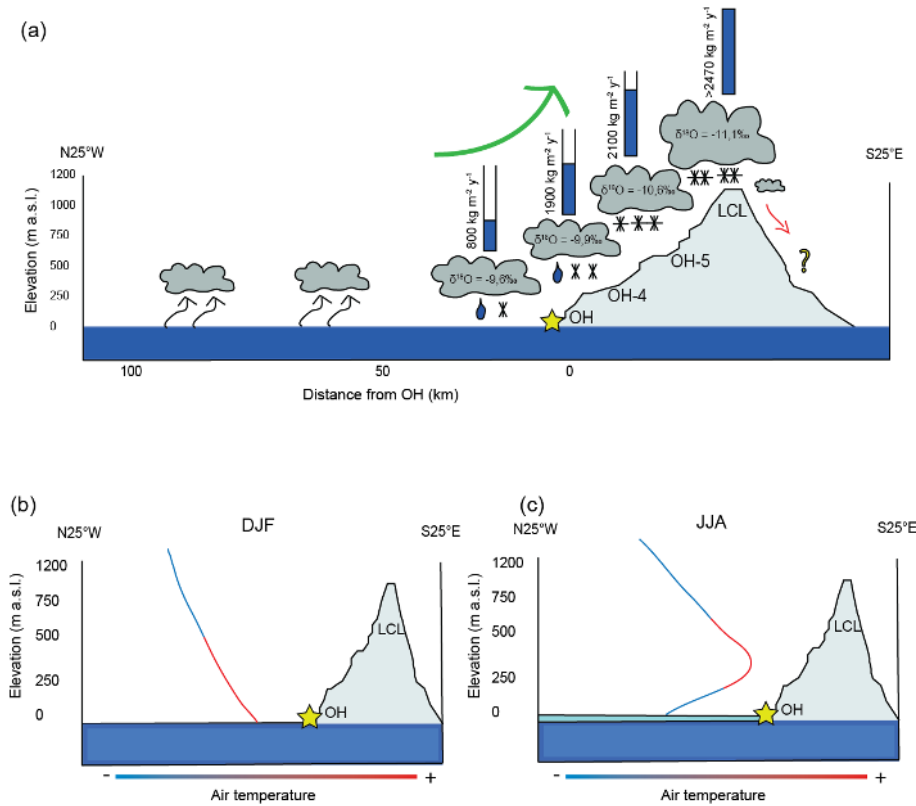
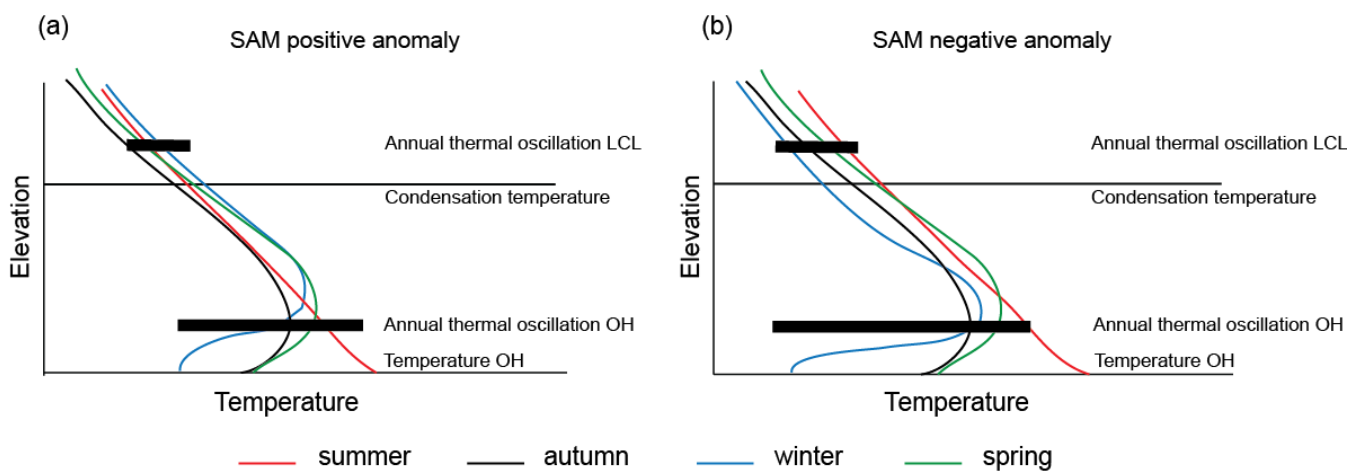


Figure 15: (a) Schematic chart showing the orographic barrier effect of the API on the stable water isotope depletion and accumulation rate at different altitudes, firn core locations (OH-4, OH-5 and OH-6) and distances from the coast (OH); (b) temperature gradient (adiabatic cooling) during DJF (summer) and sea-ice-free conditions; (c) inversion layer in the lower troposphere during sea-ice-covered conditions in JJA (winter).

10



5 **Figure 16:** Sea level to LCL temperature oscillation scheme during summer (DJF), autumn (MAM), winter (JJA) and spring under: (a) positive SAM anomaly conditions and (b) negative SAM anomaly conditions.

10

15

20



Table 1: Statistical summary of the geographical location and water stable isotope composition of all firn cores examined in this work. OH-4 and OH-5 correspond to cores retrieved on the west side of the API, whereas OH-6, OH-9 and OH-10 were retrieved at LCL on the east–west divide. All cores were analyzed in a 5 cm resolution.

Core	OH-4	OH-5	OH-6	OH-9	OH-10
Coordinates	57.80°W, 63.36°S	57.62°W, 63.38°S	57.76°W, 63.45°S	57.76°W, 63.45°S	57.76°W, 63.45°S
Altitude (m a.s.l.)	350	620	1130	1130	1130
Depth (m)	15.75	10.6	11.02	11.65	10.17
Drilling date	Jan 2009	Jan 2009	Jan 2010	Jan 2014	Jan 2015
$\delta^{18}\text{O}$ (‰)					
Mean	-10.4	-10.2	-12.0	-12.80	-12.94
Sdev	1.2	1.5	2.5	2.53	2.57
Min	-14.1	-14.2	-19.8	-23.25	-21.88
Max	-7.0	-7.2	-6.5	-8.12	-7.25
δD (‰)					
Mean	-78.9	-78.1	-91.4	-97.49	-98.81
Sdev	9.7	12.0	19.4	21.04	20.45
Min	-108.2	-111.2	-154.9	-183.80	-166.82
Max	-54.0	-52.1	-53.2	-59.62	-55.80
d_{excess} (‰)					
Mean	4.0	3.9	4.4	5.11	4.72
Sdev	1.5	1.7	2.8	1.90	2.66
Min	0.5	-0.6	-2.6	0.00	-6.50
Max	8.6	8.2	15.0	10.97	11.27
n (samples)	318	213	208	232	190

5

10

15



Table 2: Statistics of the stable water isotope composition of precipitation samples collected at OH Station on the API 2008–2009 and 2014.

Station	O'Higgins	O'Higgins
Sampling interval	Feb 2008 – Mar 2009	Apr – Nov 2014
Coordinates	63.32°S, 57.90°W	63.32°S, 57.90°W
$\delta^{18}\text{O}$ (‰)		
Mean	-9.2	-10.12
Sdev	3.33	4.39
Min	-19.4	-18.43
Max	-3.8	-1.28
δD (‰)		
Mean	-70.5	-81.86
Sdev	26.44	34.21
Min	-150.6	-148.36
Max	-21.8	-15.99
d_{excess} (‰)		
Mean	2.7	3.84
Sdev	4.15	4.67
Min	-6.6	-1.75
Max	22.3	14.70
n (samples)	139	69

Table 3: Correlation between deuterium excess ($d_{\text{excess}}^{\text{meteo}}$) values calculated from monthly mean meteorological data (SST and rh) and water stable isotope monthly means for all cores used in this study.

Core	OH-4	OH-5	OH-6	OH-9	OH-10
Time interval	Jan 2006 – Jan 2009	Mar 2007 – Jan 2009	Mar 2008 – Jan 2010	Feb 2010 – Jan 2014	Feb 2012 – Jan 2015
Corr. coefficient	0.72	0.79	0.81	0.78	0.67
p-value	<0.01	<0.01	<0.01	<0.01	<0.01



Table 4: Accumulation rates calculated for all firn cores used in this study. All rates are shown as seasonal and annual mean values with respect to the time interval covered by each core.

	API Accumulation (kg m ⁻²)				
	Western Flank		LCL		
	OH-4	OH-5	OH-6	OH-9	OH-10
DJF-MAM	1121				
JJA-SON	1300				
2006	2510				
DJF-MAM	1650	>1380			
JJA-SON	1300	1150			
2007	2950	>2530			
DJF-MAM	1130	1020	>1530		
JJA-SON	770	1050	940		
2008	1900	2070	>2470		
DJF-MAM			1090		
JJA-SON			1340		
2009			2430		
DJF-MAM			700		
JJA-SON			360		
2010			1060		
DJF-MAM			680		
JJA-SON			770		
2011			1450		
DJF-MAM			1170	1080	
JJA-SON			730	690	
2012			1900	1770	
DJF-MAM			890	930	
JJA-SON			500	690	
2013			1390	1620	
DJF-MAM				630	
JJA-SON				1050	
2014				1680	